## Chemical-space completeness: a new strategy for crystalline materials exploration

Fengyu Xie $^{1\dagger},~$ Ruoyu Wang $^{1\dagger},~$ Taoyuze Lv $^1,~$ Yuxiang Gao $^1,~$ Hongyu Wu $^2,~$ Zhicheng Zhong $^{1,~2^*}$ 

<sup>1\*</sup>College of Artificial Intelligence and Data Science, Suzhou Institute of Advanced Research, University of Science and Technology of China, 188 Ren'ai Road, Suzhou, 215123, Jiangsu, China.

<sup>2</sup>Suzhou Laboratory, 388 Ruoshui Road, Suzhou, 215123, Jiangsu, China.

\*Corresponding author(s). E-mail(s): zczhong@ustc.edu.cn;
Contributing authors: fengyu\_xie@ustc.edu.cn; ruoyuwang@ustc.edu.cn;
taoyuze.lv@ustc.edu.cn; yuxgao@ustc.edu.cn; wuhy@szlab.ac.cn;
†These authors contributed equally to this work.

#### Abstract

The emergence of deep learning has brought the long-standing goal of comprehensively understanding and exploring crystalline materials closer to reality. Yet, universal exploration across all elements remains hindered by the combinatorial explosion of possible chemical environments, making it difficult to balance accuracy and efficiency. Crucially, within any finite set of elements, the diversity of short-range bonding types and local geometric motifs is inherently limited. Guided by this chemical intuition, we propose a chemical-system-centric strategy for crystalline materials exploration. In this framework, generative models are coupled with machine-learned force fields as fast energy evaluators, and both are iteratively refined in a closed-loop cycle of generation, evaluation, and finetuning. Using the Li-P-S ternary system as a case study, we show that this approach captures the diversity of local environments with minimal additional first-principles data while maintaining structural creativity, achieving closed-loop convergence toward chemical completeness within a bounded chemical space. We further demonstrate downstream applications, including phase-diagram construction, ionic-diffusivity screening, and electronic-structure prediction. Together, this strategy provides a systematic and data-efficient framework for modeling both atomistic and electronic structures within defined chemical spaces, bridging accuracy and efficiency, and paving the way toward scalable, AI-driven discovery of crystalline materials with human-level creativity and first-principles fidelity.

**Keywords:** Chemical system, Materials discovery, Crystal structure generation, Machine-learning force-field, Crystalline materials

#### 1 Introduction

Exploring and understanding materials across the periodic table remains a grand challenge in modern materials science. The ultimate goal is to achieve universal, accurate, and efficient modeling of atomic and electronic structures for all compositions under realistic temperature and pressure conditions, spanning stable and metastable phases[1, 2], defects[3], and interfaces[4]. Such capability would transform not only materials simulation workflows but also the next-generation AI-native databases for materials design.

Recent advances in deep generative models for crystals (e.g., MatterGen[5], DiffCSP[6], ADiT[7], Uni3DAR[8]) and machine-learned force fields (MLFFs) (e.g., DPA-3[9], MatterSim[10], MACE[11], CHGNet[12]) have brought this vision closer to reality. Generative models explore latent structural spaces beyond template filling[13] or elemental substitution approaches[14, 15], and offer composition variability compared to traditional crystal-structure prediction methods[16–20]. Meanwhile, MLFFs provide near-DFT accuracy in energy and force evaluation at orders-of-magnitude lower computational cost. In principle, integrating these capabilities could yield a universal autonomous engine for structure generation, evaluation, and property prediction.

However, a fundamental challenge remains. In all-element exploration, a difficult trade-off between accuracy and efficiency arises from the vast combinatorial diversity of element combinations and bonding environments. Large foundational models such as UMA[21] exhibit impressive cross-chemistry generalizability. Yet, their universal validity across arbitrary element combinations and bonding environments, particularly in defected systems, has not been systematically established. Given their enormous training and inference cost, such large models are inefficient for most real-world research scenarios, where rapid iteration, domain-specific fine-tuning and multi-fidelity adaptation are often essential. In contrast, smaller models such as MatterSim, DPA-3, or MACE enable flexible fine-tuning and efficient inference, but often fall short of universal accuracy. Without simultaneously ensuring both efficiency and accuracy, high-throughput exploration remains fundamentally restricted. Therefore, a new strategy that enables sufficiently accurate atomistic and electronic-structure modeling at manageable computational cost is of pivotal importance.

The nature of chemical bonds itself provides key intuition. As suggested by the Materials Project[22], the majority of realistic crystalline materials can be grouped into chemical systems comprising a small (<7) and finite set of elements. Within such a chemical system, the diversity of short-range bonding types and local geometries is inherently limited by valence and coordination constraints. For instance, carbon

atoms predominantly adopt  $sp^3$ ,  $sp^2$ , or  $sp^1$  hybridization even in amorphous networks [23, 24], while silicon in silicates typically forms  $SiO_4$  tetrahedra [25]. Once these local building blocks are enumerated, the remaining structural diversity largely arises from their spatial arrangements. Together, these observations suggest that chemical-system-level completeness may be attainable without pursuing all-element universality, but rather through a divide-and-conquer strategy applied to individual chemical spaces. Achieving completeness in a target chemical space should also be sufficient in most real-world applications.

Grounded in this intuition, we introduce a chemical-system—centric strategy for crystalline materials exploration. Rather than seeking all-element universality, our framework targets chemical-space completeness, i.e., achieving structural and property coverage within a defined chemical system. This is realized through an iterative fine-tuning and active-learning loop that couples generative models and MLFFs: the generative model proposes candidate structures, the MLFF evaluates their energetics, and selected DFT data are used to refine both models (see Figure 1 and Supplementary Figure 1). By focusing on finite bonding environments and compositional boundaries, the workflow rapidly converges toward meV-level accuracy and saturates the diversity of local motifs, achieving closed-loop convergence toward chemical completeness at manageable computational cost.

We demonstrate this strategy on the Li-P-S ternary system, a prototypical yet chemically intricate solid-state electrolyte chemistry [26, 27]. Phosphorus and sulfur form diverse bonding networks, including tetrahedral PS<sub>4</sub> units, P-P-linked trigonal motifs, and bridging or polymeric sulfide species, generating complex anionic frameworks coupled to lithium coordination. This system provides a stringent test case to examine whether, despite its rich anionic diversity and glass-forming tendency, the underlying short-range chemical environments remain finite and learnable. With only  $\sim 1500$  CPU hours (32-core Xeon Gold) and  $\sim 800$  GPU hours (NVIDIA V100), our framework completed seven exploration cycles, generating 70,000 candidate structures, more than 10,000 of which are stable-unique-novel. The MLFF achieved meV-level accuracy in energy and force within just two to three iterations, and structural analysis revealed rapid saturation of local environments, suggesting a quantifiable notion of chemical completeness within the system. Notably, although the generative model was trained exclusively on existing structures from the Materials Project[2] and Alexandria databases[13, 28]—datasets often regarded as chemically comprehensive—our framework autonomously rediscovered a broad range of chemically plausible P-S anionic motifs and metastable phases beyond those databases. These include the  $(PS_3)_3^{3-}$  trimer, the  $P_3S_8^{3-}$  ring, two isomers of the  $P_2S_8^{2-}$  ring, and polymeric  $(PS_4)_n^{n-}$  chains. Their existence and internal bonding patterns, such as P–P and S-S linkages, are consistent with historical experiments, underscoring their chemical credibility. Together, these results highlight our framework's ability to creatively and rationally infer bonding rules from minimal priors and to reconstruct a more complete representation in a chemical space.

Beyond structural generation, this closed-loop strategy yields chemical-systemaccurate MLFFs and electronic structure models, thus integrates naturally with downstream property simulation workflows, including phase-diagram construction,

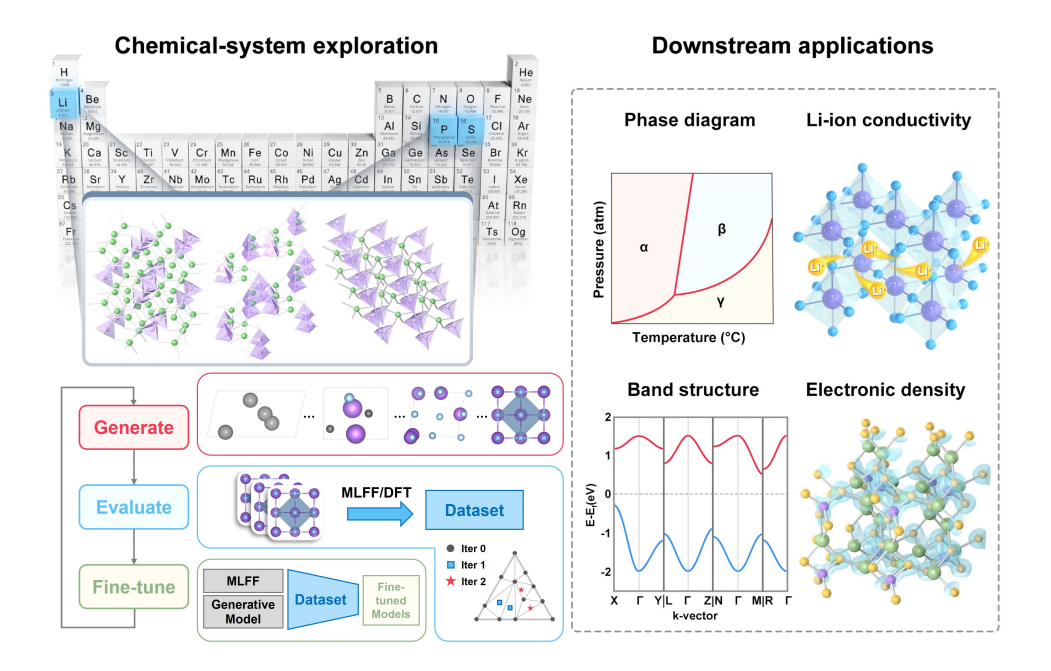


Fig. 1 Schematic of the chemical-system-centeric iterative framework for crystal structure exploration. Within a selected chemical space (for example, the Li–P–S system), deep generative models are employed to create candidate crystal structures, while machine-learned force fields (MLFFs) provide fast and accurate evaluation of their thermodynamic stability. Both models are iteratively fine-tuned on a small subset of DFT-evaluated structures, forming a closed-loop workflow that continuously refines generation and evaluation quality. The resulting candidate structures can be further coupled with downstream computations to build databases of atomistic and electronic properties across the explored chemical space.

ionic-conductivity estimation, and electronic-structure prediction, providing a coherent, multimodal solution for chemical-space exploration. In principle, this iterative generation and fine-tuning strategy can be extended to other multicomponent chemical systems and to more complex scenarios, including defects and interfaces. By grounding generative exploration in the physically finite nature of chemical systems, our strategy bridges the gap between accuracy and efficiency, laying the foundation for scalable, data-efficient, and AI-driven materials discovery and modeling pipelines.

#### 2 Results

#### 2.1 Generative model adaptiveness to energetic fine-tuning

We begin by illustrating the adaptiveness of crystal generative model to energetic fine-tuning. As shown in Figure 2a, unconditional generation, constrained only by element types, produces a wide, unimodal  $E_{\rm hull}$  distribution from -0.05 to 0.4 eV/atom (blue curve). In contrast, generations conditioned on  $E_{\rm hull}=0.0$  eV/atom yield narrower, bimodal distributions typically spanning from -0.05 to 0.3 eV/atom, with two peaks

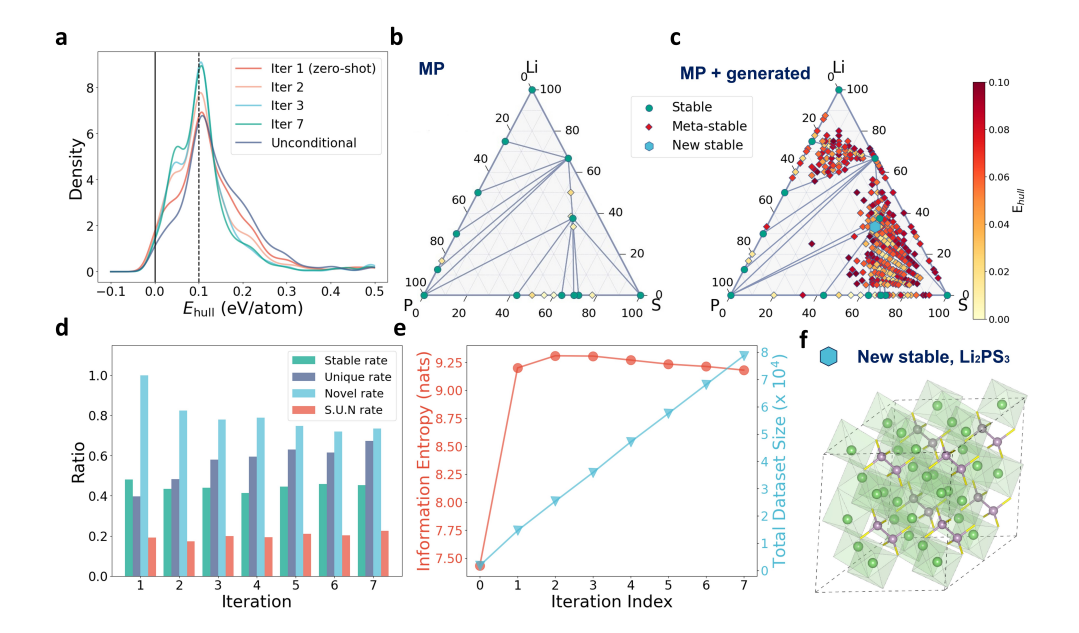


Fig. 2 (a) Density distribution of generated structures over  $E_{\rm hull}$  within the Li–P–S chemical space. (b–c) Zero-temperature phase diagrams including all Li–P–S phases from (b) the Materials Project (MP) database and (c) the MP database combined with all iteratively generated S.U.N. structures. Green circles denote stable phases on the convex hull, while the blue hexagon marks the newly discovered Li<sub>2</sub>PS<sub>3</sub> stable phase absent from MP. Yellow-to-red dots indicate metastable structures with  $E_{\rm hull} \leq 0.1~{\rm eV/atom}$ , where darker red corresponds to higher Ehull and thus lower stability. (d) Ratios of stable (green), unique (blue), novel (cyan), and total S.U.N. (red) structures as a function of iteration number. (e) Information entropy of local atomic features (red dots) and the total number of DFT calculations (cyan triangles) versus iteration number. Iteration 0 corresponds to Li–P–S structures originally included in the MP database. (f) Crystal structure of the newly generated stable Li<sub>2</sub>PS<sub>3</sub> phase, highlighted as a blue hexagon in (c).

near 0.05 and 0.1 eV/atom, respectively. Successive iterative fine-tuning on  $E_{\rm hull}$  further increases the fraction of low-energy structures, as evidenced by the growth of the minor peak near  $\sim 0.05$  eV/atom from iteration 1 to iteration 7. This trend indicates that the model gradually learns to favor configurations closer to thermodynamic stability. During this iterative search, numerous metastable structures previously unreported in the Materials Project (MP)[2, 22] were generated, and notably one new stable phase, Li<sub>2</sub>PS<sub>3</sub> with P-P bonded P<sub>2</sub>S<sub>6</sub><sup>4-</sup> anions, absent from the MP but seen in experimental studies[29, 30], was rediscovered (Figure 2b and c). These results show that conditioning the generative model on the energy-above-hull metric ( $E_{\rm hull}$ ) effectively steers the generated distribution toward lower energies over successive iterations.

## 2.2 Saturation of local chemical environments as a sign of chemical-space completeness

Despite the continuous discovery of stable–unique–novel (S.U.N.)[5] phases throughout the iterations (Figure 2d), with the ratio of S.U.N structures per iteration remaining

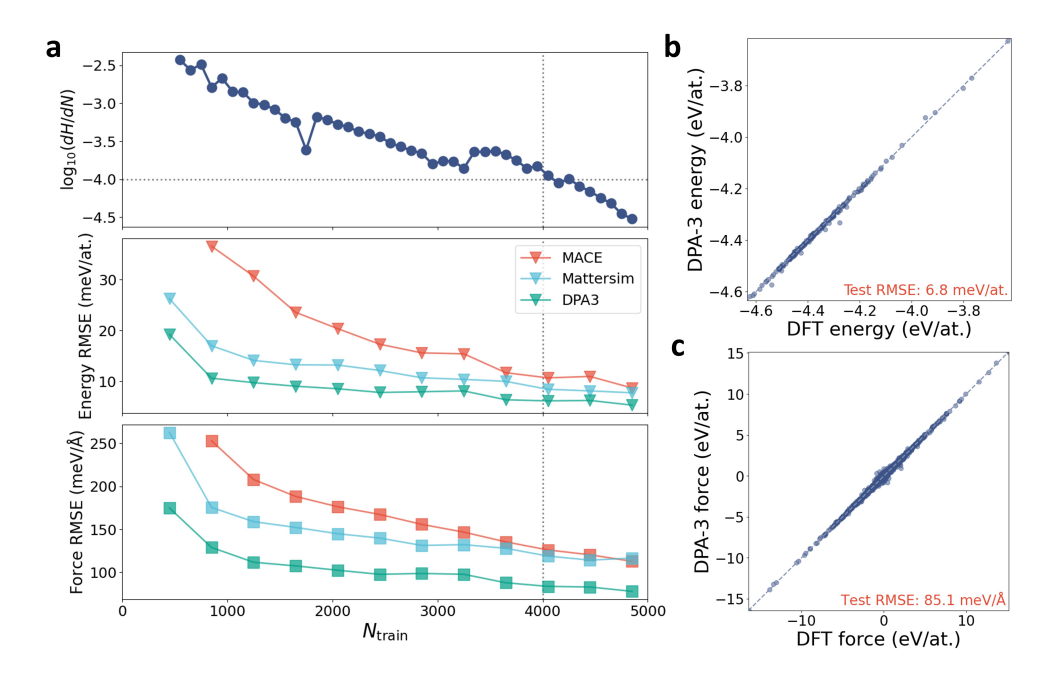


Fig. 3 Fine-tuning performance of machine-learned force fields in the Li–P–S chemical system. (a) Logarithm of the information-entropy increase rate ( $\log_{10}(dH/dN)$ , upper panel), tested energy RMSE (middle panel), and force RMSE (lower panel) as functions of the number of training frames ( $N_{\rm train}$ ).(b–c) Parity plots comparing DFT-calculated and DPA-3-predicted (b) energies and (c) forces on the test set. The DPA-3 model shown here is fine-tuned using  $N_{\rm train}=4050$ .

at approximately 18%, the information entropy[31] of generated local atomic features rapidly converges within the first two to three cycles and subsequently decreases slightly due to repeated short-range motifs (Figure 2e). Supplementary Figure 2 also shows that the distributions of first t-SNE[32] components of local structure fingerprints[33] per iteration overlap almost entirely after 2 iterations, further indicating convergence of local chemical environments. This saturation suggests that the diversity of local coordination and bonding types is largely exhausted early in the closed-loop exploration. Newly generated structures in later iterations mainly arise from spatial rearrangements or recombinations of these existing motifs rather than from genuinely new bonding patterns, even within a chemically complex system such as Li-P-S. Such behavior quantitatively supports our previous assumption of chemical-space completeness, i.e. within a finite element set, the diversity of local bonding environments is limited and learnable, justifying the feasibility of achieving near-exhaustive coverage of short-range atomic configurations in Li-P-S chemical system through iterative AI-driven exploration.

#### 2.3 Fine-tuning performance of machine-learned force fields

As the diversity of local chemical environments saturates, the machine-learned force fields (MLFFs) rapidly adapt and achieve generalization across the entire Li-P-S chemical system with only a small amount of DFT data required for fine-tuning. Fine-tuned models substantially reduce both energy and force prediction errors. Using a small number of structures selected by maximum-information-entropy-gain criteria (see Methods) for fine-tuning, we are able to construct high-quality force fields with excellent transferability. Among the compared models (DPA-3[9], MACE[11] and MatterSim[10]), DPA-3 consistently delivers the best performance (Figure 3a). At  $N_{\rm train} = 4050$  DFT frames where the entropy increase rate (dH/dN) drops below  $10^{-4}$  per structure, DPA-3 achieves an energy root-mean-square error (RMSE) of 6.8 meV/atom and a force RMSE of 85.1 meV/Å on the test set spanning the full Li-P-S chemical space (Figure 3b,c). This level of accuracy significantly improves the reliability of stability evaluation, reducing the RMSE in E<sub>hull</sub> from 46.9 to 26.5 meV/atom (Supplementary Figure 3). Encouragingly, the fine-tuning process shows diminishing reward beyond  $\sim 1000$  training frames, suggesting that  $\sim 1000$  DFT samples (or  $dH/dN < 10^{-3}$ ) is likely already sufficient for pre-screening purposes if not pursuing accurate simulations. At  $N_{\rm train} = 1250$ , the energy and force RMSEs are as low as 9.8 meV/atom and 111.5 meV/Å, respectively, providing reliable precision for largescale stability filtering and ranking of generated structures. Other chemically simpler systems are expected to require even less DFT data to achieve comparable level of accuracy.

## 2.4 Generative discovery of diverse and chemically plausible P–S anionic motifs

To assess the chemical creativity of our closed-loop workflow, we analyze the local anionic motifs emerging in the Li–P–S chemical space. Figure 4a visualizes the t-SNE distribution of local structural fingerprints of all S.U.N structures (excluding Li atoms), where colored clusters highlight representative thiophosphate anions shown in Figure 4b–m.

When compared with the MP2020 + Alexandria[13, 28] dataset (Alex-MP), on which the generative model was pretrained[5], the workflow successfully reproduces a broad range of known anionic units. These include motifs widely reported in the Li–P–S family, such as the  $PS_3^{4-}$  tetrahedron anion and  $(PS_3)_n^{n-}$  corner-sharing chains found in Li<sub>3</sub>PS<sub>4</sub> and LiPS<sub>3</sub>, as well as motifs present in other metal thiophosphates within the training set but absent from Li–P–S, for example, the  $P_2S_6^{2-}$  edge-sharing dimer, the  $P_2S_7^{4-}$  corner-sharing dimer, the  $PS_3^{2-}$  triangular monomer featuring P(IV) and the dimer  $P_2S_6^{4-}$  with a P-P bond.

Beyond these, the model also generates "imagined", ring-like and polymeric motifs that do not appear in any thiophosphate compounds within the combined training set, such as  $(PS_3)_3^{3-}$ ,  $P_3S_8^{3-}$ , two isomers of  $P_2S_8^{2-}$ , and polymeric  $(PS_4)_n^{n-}$ . Remarkably, many of these motifs correspond to species discovered early in niche experimental syntheses or spectroscopic studies of thiophosphate compounds, some (such as polymeric

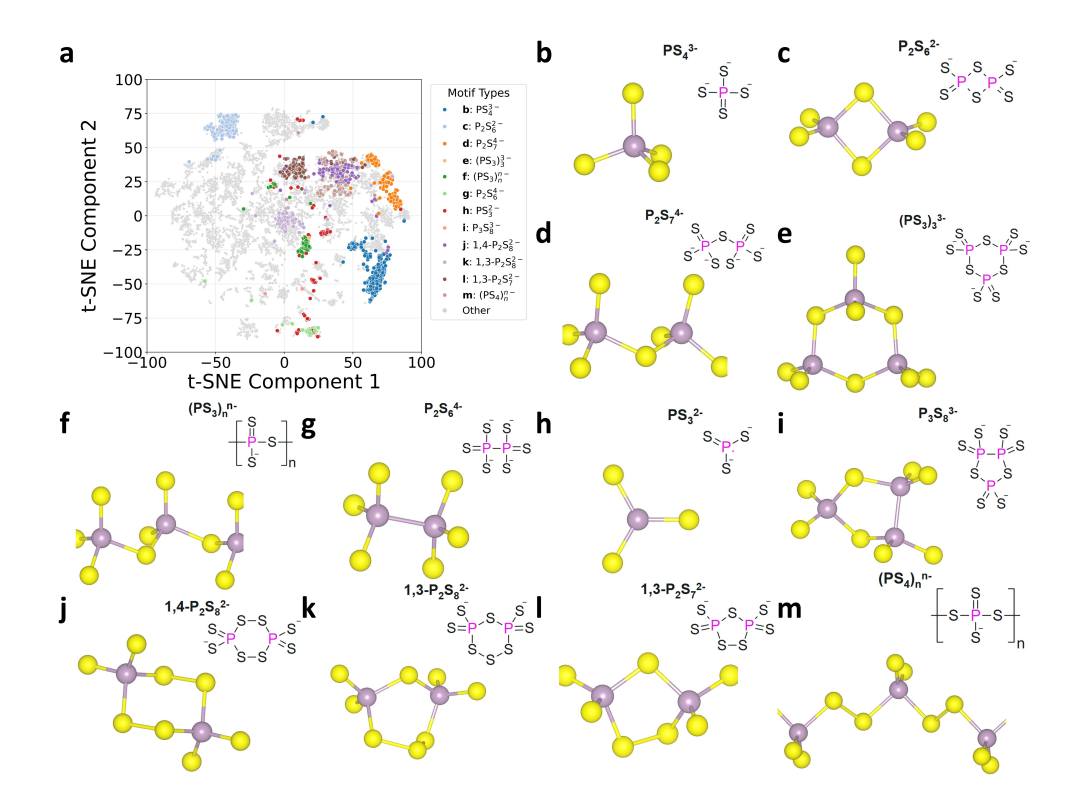


Fig. 4 Generative diversity of P–S anionic motifs in the Li–P–S chemical space. (a) Distribution of the first two t-SNE components of the local structural fingerprints of all generated structures (excluding Li atoms). Colored clusters highlight groups of structures containing representative anion motifs as shown in b-m. (b-m) Representative thiophosphate anions discovered in the iterative process. Purple and yellow spheres represent P and S atoms, respectively. (b)  $PS_4^{3-}$  tetrahedron anion. (c)  $P_2S_6^{2-}$  edge-sharing anion. (d)  $P_2S_7^{4-}$  corner-sharing anion. (e)  $P_3S_9^{3-}$  corner-sharing ring anion. (f)  $(PS_3)_n^n$  polymeric chain. (g)  $P_2S_6^{4-}$  dimer with P-P bond. (h)  $PS_3^{2-}$  triangular monomer. (i)  $P_3S_8^{3-}$  ring anion. (j) 1,4- $P_2S_8^{2-}$ , with two P atoms occupying para positions (1,4-substitution) within a sixmembered  $P_2S_4$  ring, lying opposite to each other across two S-S bridges. (k) 1,3- $P_2S_8^{2-}$ , with two P atoms occupying meta positions (1,3-substitution) within a six-membered  $P_2S_4$  ring. (l) 1,3- $P_2S_7^{2-}$ , featuring two P atoms in meta positions within a five-membered  $P_2S_3$  ring. (m)  $(PS_4)_n^{n-}$  polymeric chain linked by S-S bonds.

 $(PS_4)_n^{n-})$  even reflecting a recent designing strategy against contact loss [34], confirming the chemical plausibility, the imaginative creativity and the reasoning consistency of the generative workflow. A summary of motif occurrences is provided in Table 1, indicating which P–S anionic units are present in the training set and whether they have previously been reported in Li–P–S or other chemical systems, together with experimental references.

These findings demonstrate that the workflow:

- adaptively learns P–S, P-P and S-S bonding rules and coordination preferences directly from data;
- creatively explores new combinations of known local motifs to form chemically consistent polyanions;
- generalizes beyond its training distribution to hypothesize structures that are chemically plausible;

In summary, the model exhibits a chemist-like reasoning process—rediscovering, recombining, and rationalizing bonding motifs with human-level intuition but orders of magnitude higher efficiency.

**Table 1** Summary of representative P–S anion motifs identified in the generative exploration, their presence in the Alex–MP training dataset, and corresponding experimental references.

Formula	In Alex–MP, Li–P–S	In Alex–MP, other systems	Experimental ref.
$PS_4^{3-}$	√(Li <sub>3</sub> PS <sub>4</sub> )	√(Na <sub>3</sub> PS <sub>4</sub> , K <sub>3</sub> PS <sub>4</sub> )	[35, 36]
$P_2S_6^{2-}$	×	$\checkmark$ (KPS <sub>3</sub> , CsPS <sub>3</sub> , CuPS <sub>3</sub> , etc.)	[37-40]
$P_2S_7^{4-}$	X	$\checkmark$ (LiCrP <sub>2</sub> S <sub>7</sub> , Zn <sub>2</sub> P <sub>2</sub> S <sub>7</sub> , KVP <sub>2</sub> S <sub>7</sub> , etc.)	[41, 42]
$(PS_3)_3^{3-}$	×	×	[39, 43, 44]
$(PS_3)_n^{n-}$	$\checkmark(\text{LiPS}_3)$	$\checkmark(KPS_3, CuPS_3)$	[41, 45, 46]
$P_2S_6^{4-}$	X	$\checkmark$ (LiAlP <sub>2</sub> S <sub>6</sub> , MnPS <sub>3</sub> , MgPS <sub>3</sub> , etc.)	[29, 30]
$PS_3^{2-}$	X	$\sqrt{(K_2CdP_2S_6, Cs_3NaP_2S_6, etc.)}$	[29]
$P_3S_8^{3-}$	X	×	[44]
$1,4-P_2S_8^{2-}$	×	×	[44, 47, 48]
$1,3-P_2S_8^{2}$	X	×	[49]
$1,3-P_2S_7^{2}$	×	×	[44, 50]
$(\mathrm{PS}_4)_n^{n-1}$	×	×	[34]

## 2.5 Downstream applications: P-T phase stability in the Li-P-S chemical space

Our trained MLFF enables quantitative phase diagram construction by incorporating finite-pressure effects and thermally activated lattice vibrations through the quasi-harmonic approximation [51].

Figure 5a–c shows the computed P–T phase stability diagrams of the Li–P–S chemical system under varied thermodynamic conditions. Comparing Figure 5a and b, the impact of increasing temperature (from 300 K to 600 K at 1 bar) on phase stability is relatively minor, with only a slight increase in  $E_{\rm hull}$  for low-Li compositions near the P–S boundary. In contrast, pressure exerts a much stronger influence. At 2 GPa (Figure 5c), phases with S content above 50 at.% (points near the S corner) become significantly less stable, primarily due to lower atomic packing densities, which increases the PV contributions to the Gibbs free energy (see Supplementary Figure 4a).

Throughout these thermodynamic conditions, Li<sub>2</sub>PS<sub>3</sub> and Li<sub>3</sub>PS<sub>4</sub> remain thermodynamically stable over a broad range of temperatures and pressures (300–600

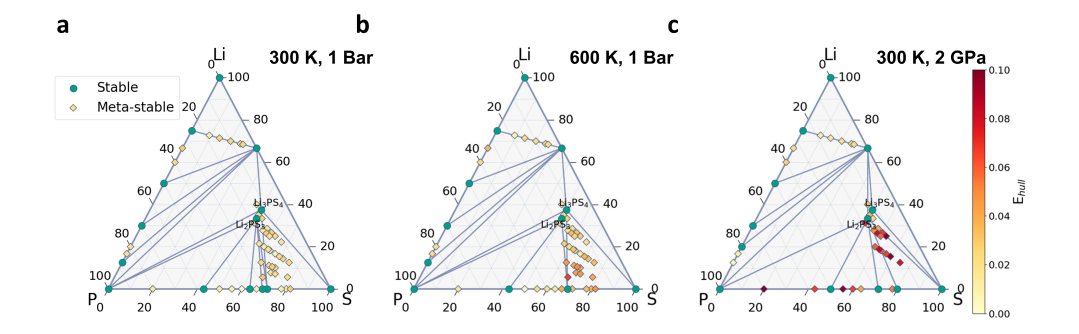


Fig. 5 Finite temperature-pressure phase diagrams in Li-P-S chemical space at varied temperatures and pressures. (a) Phase diagram at T = 300 K, P = 1 bar. (b) Phase diagram at T = 600 K, P = 1 bar. (c) Phase diagram at T=300 K, P=2 GPa. Green dots represent stable phases on the convex hull, while triangles represent metastable phases with  $E_{\rm hull} < 0.1$  eV/atom, and darker red color indicates lower stability.

K, 1 bar–2 GPa). The characteristic  $P_2S_6^{4-}$  and  $PS_4^{3-}$  anionic units persist, whereas their preferred spatial arrangements evolve subtly with temperature and pressure (see Supplementary Figure 4b-e). These results demonstrate that our proposed framework can yield accurate, fine-tuned MLFFs capable of capturing finite-temperature, finite-pressure thermodynamics within a chemical system.

#### 2.6 Downstream applications: Ionic-conductivity screening

Using the trained MLFF, we performed high-throughput molecular dynamics (MD) simulations at 700 K for 60 ps to pre-screen potential solid-state electrolyte (SSE) candidates from iteratively generated structures. Prior to MD, structures were filtered by composition and stability criteria:  $x_{\rm Li} > 0.15, x_{\rm P} > 0, x_{\rm S} > 0.45, E_{\rm hull} \leq 0.03$  eV/atom, and specific volume per Li atom  $< 200 {\rm \AA}^3$ . To exclude kinetically unstable phases (e.g., those that undergo structural transformation or chemical decomposition), we further require diffusivities of P and S to be below  $10^{-6}~{\rm cm}^2/{\rm s}$  and require the Li-ion conductivity ( $\sigma_{\rm Li} = n_{\rm Li} q^2 D_{\rm Li}/(k_{\rm B}T)$ ) to be higher than 400 mS/cm.

From this screening, 29 Li-ion conductor candidates outside of the MP database were identified (see Supplementary Table 1 and Supplementary Figure 5). Figure 6a shows that highly conductive phases tend to exhibit slightly elevated  $E_{\rm hull}$  values relative to non-conducting counterparts, echoes the empirical design principle[52] that moderate energetic metastability can facilitate local lattice fluctuations and provide low-barrier migration channels for Li<sup>+</sup> transport.

Figure 6b compares the mean-squared displacement (MSD) of Li ions between the newly identified on-hull P43m Li<sub>3</sub>PS<sub>4</sub> phase (Figure 6d) and a metastable  $\alpha$ -like Li<sub>3</sub>PS<sub>4</sub> structure[36](Figure 6e). In the P43m phase, all PS<sub>4</sub><sup>3-</sup> tetrahedra align in parallel, generating symmetric Li sites that stabilize Li<sup>+</sup> ions and suppress diffusion. In contrast, the  $\alpha$ -like phase exhibits alternating PS<sub>4</sub><sup>3-</sup> orientations along the c-axis, lowering local symmetry, raising Li-site energy and promoting intersite hopping. This structural contrast implies a potential microscopic explanation for the wide

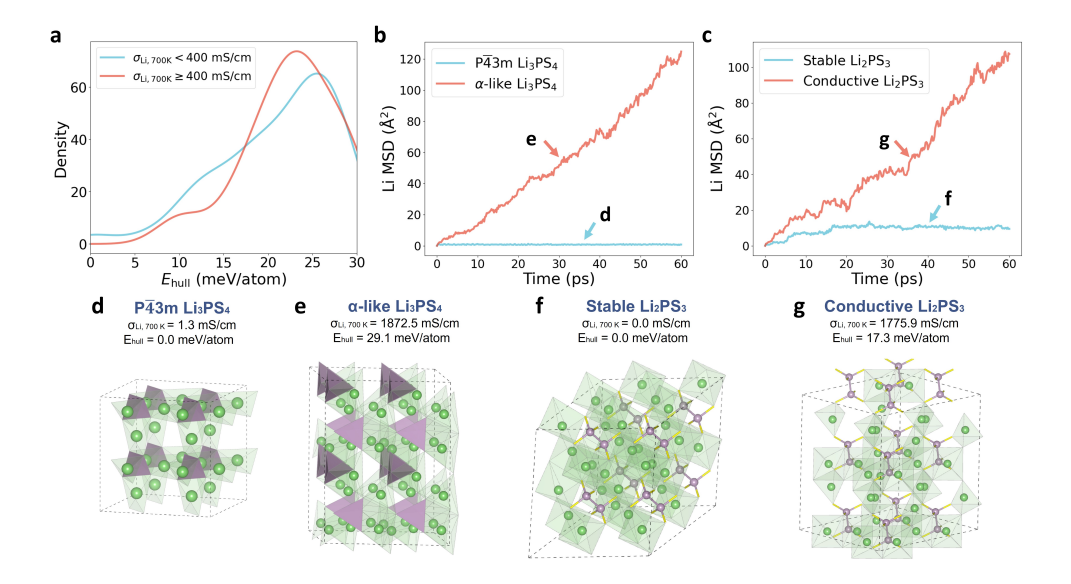


Fig. 6 Ionic-conductivity screening results. (a) Distribution densities of kinetically stable Li-ion conductors (red,  $\sigma_{\text{Li}} \geq 400 \text{ mS/cm}$ ) and insulators (cyan,  $\sigma_{\text{Li}} < 400 \text{ mS/cm}$ ) over  $E_{\text{hull}}$ . (b-c) Li MSD at 700 K as a function of simulation time in example (b) Li<sub>3</sub>PS<sub>4</sub> and (c) Li<sub>2</sub>PS<sub>3</sub> polymorphs. Red curves indicate the metastable conductive polymorph, whereas cyan curves represent the most stable version. (d-g) Crystal structures of the example polymorphs. (d) P̄43m Li<sub>3</sub>PS<sub>4</sub>. (e)  $\alpha$ -like Li<sub>3</sub>PS<sub>4</sub>. (f) Stable Li<sub>2</sub>PS<sub>3</sub>. (g) Conductive Li<sub>2</sub>PS<sub>3</sub>. These structures were identified through iterative exploration and are absent from the MP database.

range of experimentally reported Li<sub>3</sub>PS<sub>4</sub> conductivities [53–55], as the coexistence of low- and high-symmetry domains may disrupt long-range conduction pathways, while their relative fraction may vary under different synthesis conditions and thus different amorphization extent. Similarly, Figure 6c compares the most stable Li<sub>2</sub>PS<sub>3</sub> phase (Figure 6f) with its most conductive polymorph (Figure 6g). The stable phase confines all Li ions to octahedral sites, whereas the conductive variant accommodates half of the Li in tetrahedral environments, substantially enhancing Li-ion mobility.

We note that some of the predicted high-conductivity candidates, such as  $\rm Li_2PS_3$ , have been experimentally reported to exhibit limited ionic transport at ambient conditions [30]. This discrepancy likely arises from the fact that our MD-based screening is performed at elevated temperature (700 K) and short timescales, which primarily capture intrinsic lattice-mobility trends rather than experimentally accessible conductivities. Therefore, these predictions should be viewed as indicators of potential mobility channels rather than quantitative room-temperature values. Together, these results demonstrate that the proposed workflow can automatically identify stable yet structurally diverse ionic conductors, offering a general strategy for large-scale SSE discovery across chemical systems.

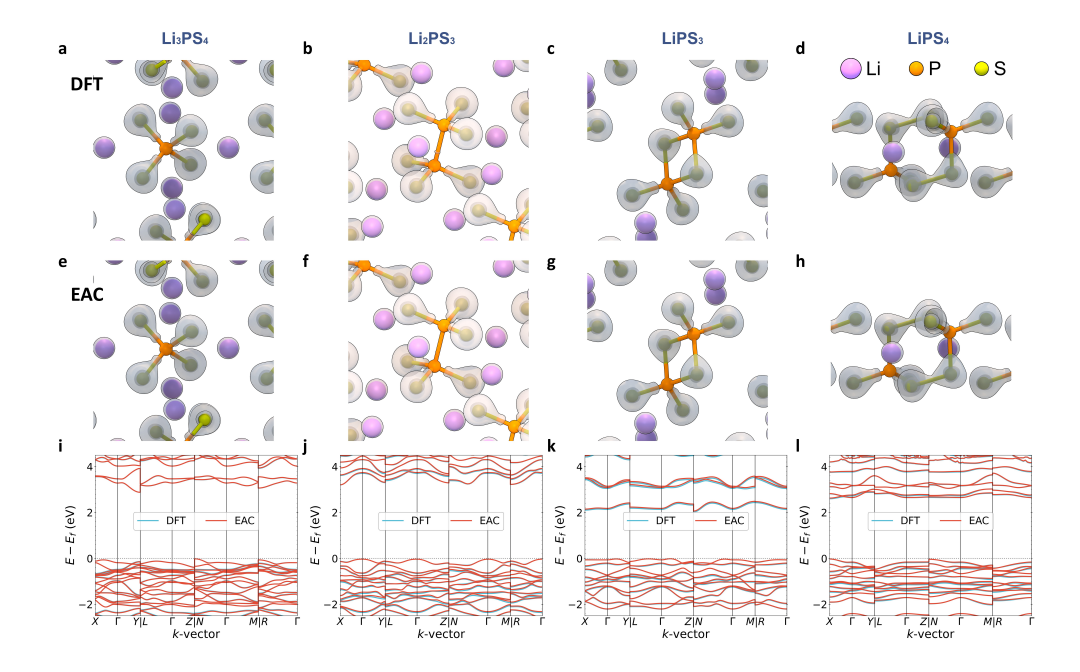


Fig. 7 Electronic-structure prediction results. (a–h) Comparison of electronic charge densities for representative structures: (a, e) Li<sub>2</sub>PS<sub>4</sub>, (b, f) Li<sub>2</sub>PS<sub>3</sub>, (c, g) Li<sub>2</sub>PS<sub>3</sub>, and (d, h) Li<sub>2</sub>PS<sub>4</sub>. Panels a–d show charge densities obtained from self-consistent DFT calculations, while panels e–h display those predicted by the fine-tuned EAC-Net. (i–l) Electronic band-structure dispersions of the aforementioned representative compounds: (i) Li<sub>3</sub>PS<sub>4</sub>, (j) Li<sub>2</sub>PS<sub>3</sub>, (k) Li<sub>2</sub>PS<sub>3</sub>, and (l) Li<sub>2</sub>PS<sub>4</sub>. Cyan lines denote the DFT self-consistent (SCF) results, and red lines indicate non-self-consistent (NSCF) band structures computed using EAC-Net–predicted charge densities as input.

#### 2.7 Downstream applications: Electronic-structure prediction

As a demonstration beyond atomistic modeling, we further advance to the electronic-structure level by integrating a fine-tuned EAC-Net model[56] into our workflow. This addition enables efficient prediction of electronic charge density and band structure for all structures generated within the closed-loop exploration, establishing a unified framework that consistently bridges atomistic and electronic representations.

Figures 7a–d and e-h compare the DFT-computed electronic charge densities with those predicted by EAC-Net, showing excellent qualitative and quantitative agreement. Using the normalized mean absolute error (NMAE) as an accuracy metric (see Methods), EAC-Net achieves an NMAE of  $\sim 7.2 \times 10^{-3}$  at zero-shot inference, which further improves to  $\sim 4.8 \times 10^{-3}$  after fine-tuning on only 34 self-consistent-field (SCF) calculation frames (Supplementary Figure 6e), showing EAC-Net to effectively generalize across diverse chemical compositions and bonding environments within the Li–P–S system.

Furthermore, when the ML-predicted charge densities are used as inputs for non-self-consistent (NSCF) electronic band structure calculations, the resulting band

dispersions closely reproduce DFT SCF results (Figures 7i–l), while drastically reducing the computational cost. The model captures both the global band gap position and fine features near the Fermi level, indicating accurate reconstruction of the underlying electronic landscape.

These results highlight the capability of our chemical-system—centric strategy to not only generate and evaluate atomic structures efficiently, but also to infer their electronic characteristics with high fidelity, providing a unified deep-learning framework that models a full hierarchy from chemical composition and crystal geometry to charge density and electronic structure.

#### 3 Discussion

Achieving accurate and efficient modeling is essential for AI-based computational methods to meaningfully transform modern materials science. However, balancing accuracy and efficiency in high-throughput exploration remains challenging. To address this, we propose a chemical-system–centric strategy for crystalline materials exploration, integrating generative models and MLFFs into an iterative, active-learning loop. Rather than pursuing all-element universality, this closed-looped framework focus on a target chemical system. Deep generative models provide flexibility to explore varied compositions compared with conventional crystal-structure prediction methods, while MLFFs enable accurate and orders of magnitude more efficient evaluation of candidate structures. Through iterative generation and fine-tuning, the workflow attains convergence toward chemical-system-level completeness in short-range atomic environments.

We validated this strategy in the Li–P–S ternary system. Despite its apparent complexity, the exploration rapidly converged: local structural motifs saturated after the early iterations, and the MLFF reached meV-level accuracy in energy and force using only  $\sim\!4000$  DFT-labeled structures. Even in such a chemically rich space, the diversity of short-range bonding environments proved finite and learnable, allowing data-efficient coverage of the full chemical system.

Remarkably, although the Materials Project and Alexandria databases are widely regarded as chemically comprehensive, they remain incomplete as many plausible bonding motifs and metastable structures are absent. Our framework, starting from this limited prior knowledge, autonomously reconstructed much of the missing chemical information. It rediscovered one missing stable phase, the P–P–bonded Li<sub>2</sub>PS<sub>3</sub>, along with a diverse set of chemically consistent P–S anionic motifs such as the  $(PS_3)_3^{3-}$  corner-shared trimer, the  $P_3S_8^{3-}$  ring, two isomers of the  $P_2S_8^{2-}$  ring, and the polymeric  $(PS_4)_n^{n-}$  chain. These motifs are absent from the training data but supported by historical experiments, underscoring both their chemical credibility and the framework's creativity to infer realistic bonding rules. By filling these knowledge gaps within a chemically rich yet bounded system, our approach demonstrates how chemical-system–centric exploration can move beyond the limitations of current databases to establish a more complete and physically grounded representation of materials space.

Overall, our strategy unifies generative creativity, modeling accuracy, and computational efficiency, enabling self-consistent generation and evaluation of chemically plausible crystal structures.

In addition, as the iterative generation loop saturates the diversity of local short-range environments, our framework converges toward chemical-system-complete MLFFs and electronic structure models (e.g., EAC-Net) for crystalline materials within bounded chemical spaces. These models naturally integrate with downstream applications such as finite-temperature and finite-pressure phase diagrams, ionic-conductivity screening, and electronic-structure analysis. Collectively, these components form a coherent solution for chemical-space-level exploration, offering a shift from costly, resource-intensive universal strategies toward physically grounded and practically scalable frameworks. Looking forward, this strategy can, in principle, be extended to other multi-component chemical systems and adapted to more complex scenarios of practical interest, such as defects and interfaces, providing a unified route to address increasingly realistic materials problems.

By grounding materials discovery in chemical-system completeness rather than all-element universality, this work redefines the practical scope and scalability of computational materials science. It establishes a systematic, autonomous, and physically grounded framework for exploring atomic and electronic landscapes with first-principles fidelity, paving the way toward next-generation AI-native materials discovery that unifies structures, properties, and electronic information within a self-refining computational ecosystem.

#### 4 Methods

#### 4.1 Generative model

We primarily employed MatterGen[5] as the generative backbone due to its built-in support for complex conditional generation, while other crystal generation models such as Con-CDVAE[57], ADiT[7], and Uni3DAR[8] can in principle be adapted within the same framework.

Starting from the open-source,  $E_{\rm hull}$ - and chemical-system-conditional version [58] of MatterGen, we generated 9,984 candidate structures per iteration—3,328 for each conditioned  $E_{\rm hull}$  (0.00, 0.03, and 0.06 eV/atom). Preliminary relaxations were conducted using the MLFF, and  $E_{\rm hull}$  values were evaluated relative to the MP database and previously generated structures.

S.U.N. structures were selected following the same criteria in the original Matter-Gen work:

- Stability:  $E_{hull} < 0.1 \text{ eV/atom.}$
- Uniqueness: no identical structure within the current iteration, identified by pymatgen's [59] Structure Matcher.
- Novelty: not present in earlier iterations or in the MP database, also verified using StructureMatcher.

After DFT evaluation, the generative model was fine-tuned using ground-truth DFT-computed  $E_{\rm hull}$  values to incorporate newly sampled chemical motifs and bias subsequent generations toward lower-energy configurations.

#### 4.2 DFT computations and dataset preparation

In each iteration, up to 600 MLFF-relaxed structures were selected for DFT calculations according to  $E_{\rm hull}$  intervals:  $\leq 100$  for  $E_{\rm hull} < 0$ , 200 for  $0 \leq E_{\rm hull} < 0.03$ , and 300 for  $0.03 \leq E_{\rm hull} < 0.10$  eV/atom. Typically 400–600 structures were sampled. Each structure was randomly perturbed three times in atomic coordinates and lattice parameters before DFT relaxation. From each trajectory, 1–5 ionic steps, including the initial and final states, were randomly extracted.

To enrich the dataset, five additional static calculations were performed on random perturbations of each converged structure, producing a set of compositionally and structurally diverse configurations with corresponding energies and forces. Each iteration yielded roughly 10,000 data points. The perturbation amplitudes followed normal distributions of 0.08–0.15 a for atomic positions (where  $a = (V_{\rm cell}/N_{\rm atom})^{1/3}$ ) and 3–5 % for lattice constants.

All DFT calculations, including structural relaxations and static perturbations, were carried out using VASP with the projector-augmented-wave (PAW) method[60–62] and the Perdew-Burke-Ernzerhof (PBE) exchange–correlation functional[63, 64]. Input files were generated using pymatgen's MPRelaxSet with default parameters. A plane-wave cutoff of 520 eV and a  $\Gamma$ -centered k-point mesh with a reciprocal-space density of 64 Å were used. Li 1s electrons were treated as valence electrons. Electronic convergence was set to  $5 \times 10^{-5}$  eV/atom, and ionic steps were converged to 10 times the electronic threshold.

To ensure internal consistency, all Li–P–S structures queried from the MP database (referred to as iteration 0) were recalculated under identical DFT settings.

#### 4.3 MLFFs

We benchmarked our framework using three MLFF architectures of comparable million-parameter size: DPA 3.1-3M[65], MACE-MPA-0-medium[66] and Mattersim-5M[67]. The neighbor cutoff radii were set to  $6\mathring{A}$  for DPA-3 and mattersim, and  $5\mathring{A}$  for MACE.

For DPA-3, models were trained for approximately 50 epochs (corresponding to  $\sim 50 \times N_{\rm train}$  steps) with automatic batch sizing. The learning rate started at 0.001 and decayed exponentially every 2000 steps to  $3 \times 10^{-5}$ . The total loss combined energy, force and virial terms with gradually adjusted mixing ratio, starting at 0.2:100:0.02 and ending at 20:60:1.

For MatterSim, training was performed for 200 epochs, with an initial learning rate of 0.001 that decayed by a factor 0.8 every 4 epochs.

For MACE, models were first trained for 400 epochs under the exponential moving average (EMA) mode, starting at a learning rate of 0.01 that decayed by 0.8 every 20 epochs once the validation plateaued followed by 100 in the stochastic weight averaging (SWA) mode at a fixed learning rate of 0.001. The validation fraction was set to 5%.

In each iteration, training structures were selected according to the maximum-information-entropy-gain criterion. Following Reference [31], information entropy of a set of n structures (H) is defined as

$$H(\{\mathbf{X}\}) = -\frac{1}{n} \sum_{i=1}^{N} \log \left[ \frac{1}{n} \sum_{j=1}^{N} K_h(\mathbf{X}_i, \mathbf{X}_j) \right]$$
(1)

where  $\mathbf{X}_i$  denotes the vectorized local atomic features of structure i,  $K_h$  is a Gaussian kernel, and h is a tunable bandwidth (default value used). The differential entropy gain upon adding a new data point  $\mathbf{Y}$  into the existing dataset  $\{\mathbf{X}\}$  is given by

$$\delta H(\mathbf{Y}|\{\mathbf{X}\}) = -\log \left[ \sum_{i=1}^{n} K_h(\mathbf{Y}, \mathbf{X}_i) \right].$$
 (2)

All DFT-labeled structures were ranked by  $\delta H$ , and the top  $N_{\rm train}$  configurations were selected to maximize the information diversity of the training set while minimizing computational cost. Training data were drawn only from iterations 0 to 3, whereas the unselected data from these iterations, along with all data from subsequent iterations, were reserved for testing. As DPA-3 models consistently achieve the best testing accuracy, we used the DPA-3 model at  $N_{train}=4050$  in subsequent stability estimation and phase-diagram computations.

**Acknowledgements.** This work was supported by the National Key R&D Program of China (Grants No. 2021YFA0718900) and National Nature Science Foundation of China (Grants No. 92477114 and No. 12374096). We thank DP Technology for providing computational resources through the Bohrium platform and data hosting services via AIS Square.

#### Declarations

The authors declare no conflict of interest.

#### References

- [1] Curtarolo, S., Hart, G.L.W., Nardelli, M.B., Mingo, N., Sanvito, S., Levy, O.: The high-throughput highway to computational materials design. Nature Materials 12(3), 191–201 (2013) https://doi.org/10.1038/nmat3568
- [2] Jain, A., Ong, S.P., Hautier, G., Chen, W., Richards, W.D., Dacek, S., Cholia, S., Gunter, D., Skinner, D., Ceder, G., Persson, K.A.: Commentary: The Materials Project: A materials genome approach to accelerating materials innovation. APL Materials 1(1), 011002 (2013) https://doi.org/10.1063/1.4812323

- [3] Freysoldt, C.: First-principles calculations for point defects in solids. Reviews of Modern Physics 86(1), 253–305 (2014) https://doi.org/10.1103/RevModPhys.86. 253
- [4] Harmer, M.P.: The Phase Behavior of Interfaces. Science 332(6026), 182–183
   (2011) https://doi.org/10.1126/science.1204204
- [5] Zeni, C., Pinsler, R., Zügner, D., Fowler, A., Horton, M., Fu, X., Wang, Z., Shysheya, A., Crabbé, J., Ueda, S., Sordillo, R., Sun, L., Smith, J., Nguyen, B., Schulz, H., Lewis, S., Huang, C.-W., Lu, Z., Zhou, Y., Yang, H., Hao, H., Li, J., Yang, C., Li, W., Tomioka, R., Xie, T.: A generative model for inorganic materials design. Nature, 1–3 (2025) https://doi.org/10.1038/s41586-025-08628-5
- [6] Jiao, R., Huang, W., Lin, P., Han, J., Chen, P., Lu, Y., Liu, Y.: Crystal Structure Prediction by Joint Equivariant Diffusion on Lattices and Fractional Coordinates. In: Workshop on "Machine Learning for Materials" ICLR 2023 (2023)
- [7] Joshi, C.K., Fu, X., Liao, Y.-L., Gharakhanyan, V., Miller, B.K., Sriram, A., Ulissi, Z.W.: All-atom Diffusion Transformers: Unified generative modelling of molecules and materials. In: Forty-Second International Conference on Machine Learning (2025)
- [8] Lu, S., Lin, H., Yao, L., Gao, Z., Ji, X., E, W., Zhang, L., Ke, G.: Uni-3DAR: Unified 3D Generation and Understanding via Autoregression on Compressed Spatial Tokens. arXiv (2025). https://doi.org/10.48550/arXiv.2503.16278
- [9] Zhang, D., Peng, A., Cai, C., Li, W., Zhou, Y., Zeng, J., Guo, M., Zhang, C., Li, B., Jiang, H., Zhu, T., Jia, W., Zhang, L., Wang, H.: Graph Neural Network Model for the Era of Large Atomistic Models. arXiv (2025). https://doi.org/10. 48550/arXiv.2506.01686
- [10] Yang, H., Hu, C., Zhou, Y., Liu, X., Shi, Y., Li, J., Li, G., Chen, Z., Chen, S., Zeni, C., Horton, M., Pinsler, R., Fowler, A., Zügner, D., Xie, T., Smith, J., Sun, L., Wang, Q., Kong, L., Liu, C., Hao, H., Lu, Z.: MatterSim: A Deep Learning Atomistic Model Across Elements, Temperatures and Pressures. arXiv (2024). https://doi.org/10.48550/arXiv.2405.04967
- [11] Batatia, I., Kovacs, D.P., Simm, G., Ortner, C., Csanyi, G.: MACE: Higher Order Equivariant Message Passing Neural Networks for Fast and Accurate Force Fields. In: Advances in Neural Information Processing Systems, vol. 35, pp. 11423–11436 (2022)
- [12] Deng, B., Zhong, P., Jun, K., Riebesell, J., Han, K., Bartel, C.J., Ceder, G.: CHGNet as a pretrained universal neural network potential for charge-informed atomistic modelling. Nature Machine Intelligence 5(9), 1031–1041 (2023) https://doi.org/10.1038/s42256-023-00716-3

- [13] Schmidt, J., Wang, H.-C., Cerqueira, T.F.T., Botti, S., Marques, M.A.L.: A dataset of 175k stable and metastable materials calculated with the PBEsol and SCAN functionals. Scientific Data 9(1), 64 (2022) https://doi.org/10.1038/s41597-022-01177-w
- [14] Hautier, G., Fischer, C., Ehrlacher, V., Jain, A., Ceder, G.: Data Mined Ionic Substitutions for the Discovery of New Compounds. Inorganic Chemistry **50**(2), 656–663 (2011) https://doi.org/10.1021/ic102031h
- [15] Merchant, A., Batzner, S., Schoenholz, S.S., Aykol, M., Cheon, G., Cubuk, E.D.: Scaling deep learning for materials discovery. Nature 624(7990), 80–85 (2023) https://doi.org/10.1038/s41586-023-06735-9
- [16] Pickard, C.J., Needs, R.J.: Ab initio random structure searching. Journal of Physics: Condensed Matter  $\bf 23(5)$ , 053201 (2011) https://doi.org/10.1088/0953-8984/23/5/053201
- [17] Oganov, A.R., Glass, C.W.: Crystal structure prediction using *ab initio* evolutionary techniques: Principles and applications. The Journal of Chemical Physics **124**(24), 244704 (2006) https://doi.org/10.1063/1.2210932
- [18] Glass, C.W., Oganov, A.R., Hansen, N.: USPEX—Evolutionary crystal structure prediction. Computer Physics Communications 175(11-12), 713–720 (2006) https://doi.org/10.1016/j.cpc.2006.07.020
- [19] Wang, Y., Lv, J., Zhu, L., Ma, Y.: Crystal structure prediction via particle-swarm optimization. Physical Review B 82(9), 094116 (2010) https://doi.org/10.1103/ PhysRevB.82.094116
- [20] Wang, Y., Lv, J., Zhu, L., Ma, Y.: CALYPSO: A method for crystal structure prediction. Computer Physics Communications 183(10), 2063–2070 (2012) https://doi.org/10.1016/j.cpc.2012.05.008
- [21] Wood, B.M., Dzamba, M., Fu, X., Gao, M., Shuaibi, M., Barroso-Luque, L., Abdelmaqsoud, K., Gharakhanyan, V., Kitchin, J.R., Levine, D.S., Michel, K., Sriram, A., Cohen, T., Das, A., Rizvi, A., Sahoo, S.J., Ulissi, Z.W., Zitnick, C.L.: UMA: A Family of Universal Models for Atoms. arXiv (2025). https://doi.org/10.48550/arXiv.2506.23971
- [22] Horton, M.K., Huck, P., Yang, R.X., Munro, J.M., Dwaraknath, S., Ganose, A.M., Kingsbury, R.S., Wen, M., Shen, J.X., Mathis, T.S., Kaplan, A.D., Berket, K., Riebesell, J., George, J., Rosen, A.S., Spotte-Smith, E.W.C., McDermott, M.J., Cohen, O.A., Dunn, A., Kuner, M.C., Rignanese, G.-M., Petretto, G., Waroquiers, D., Griffin, S.M., Neaton, J.B., Chrzan, D.C., Asta, M., Hautier, G., Cholia, S., Ceder, G., Ong, S.P., Jain, A., Persson, K.A.: Accelerated data-driven materials science with the Materials Project. Nature Materials (2025) https://doi.org/10.1038/s41563-025-02272-0

- [23] Robertson, J.: Amorphous carbon. Advances in Physics 35(4), 317–374 (1986) https://doi.org/10.1080/00018738600101911
- [24] Robertson, J., O'Reilly, E.P.: Electronic and atomic structure of amorphous carbon. Physical Review B **35**(6), 2946–2957 (1987) https://doi.org/10.1103/PhysRevB.35.2946
- [25] Liebau, F.: Structural Chemistry of Silicates. Springer, Berlin, Heidelberg (1985). https://doi.org/10.1007/978-3-642-50076-3
- [26] Sakuda, A., Hayashi, A., Tatsumisago, M.: Sulfide Solid Electrolyte with Favorable Mechanical Property for All-Solid-State Lithium Battery. Scientific Reports 3(1), 2261 (2013) https://doi.org/10.1038/srep02261
- [27] Zhang, Q., Cao, D., Ma, Y., Natan, A., Aurora, P., Zhu, H.: Sulfide-Based Solid-State Electrolytes: Synthesis, Stability, and Potential for All-Solid-State Batteries. Advanced Materials 31(44), 1901131 (2019) https://doi.org/10.1002/ adma.201901131
- [28] Schmidt, J., Hoffmann, N., Wang, H.-C., Borlido, P., Carriço, P.J.M.A., Cerqueira, T.F.T., Botti, S., Marques, M.A.L.: Machine-Learning-Assisted Determination of the Global Zero-Temperature Phase Diagram of Materials. Advanced Materials 35(22), 2210788 (2023) https://doi.org/10.1002/adma.202210788
- [29] Mercier, R., Malugani, J.P., Fahys, B., Douglande, J., Robert, G.: Synthese, structure cristalline et analyse vibrationnelle de l'hexathiohypodiphosphate de lithium Li4P2S6. Journal of Solid State Chemistry 43(2), 151–162 (1982) https://doi.org/10.1016/0022-4596(82)90224-9
- [30] Dietrich, C., Sadowski, M., Sicolo, S., Weber, D.A., Sedlmaier, S.J., Weldert, K.S., Indris, S., Albe, K., Janek, J., Zeier, W.G.: Local Structural Investigations, Defect Formation, and Ionic Conductivity of the Lithium Ionic Conductor Li<sub>4</sub> P<sub>2</sub> S<sub>6</sub>. Chemistry of Materials 28(23), 8764–8773 (2016) https://doi.org/10.1021/acs.chemmater.6b04175
- [31] Schwalbe-Koda, D., Hamel, S., Sadigh, B., Zhou, F., Lordi, V.: Model-free estimation of completeness, uncertainties, and outliers in atomistic machine learning using information theory. Nature Communications **16**(1), 4014 (2025) https://doi.org/10.1038/s41467-025-59232-0
- [32] Maaten, L., Hinton, G.: Visualizing Data using t-SNE. Journal of Machine Learning Research 9(86), 2579–2605 (2008)
- [33] Zimmermann, N.E.R., Jain, A.: Local structure order parameters and site fingerprints for quantification of coordination environment and crystal structure similarity. RSC Advances 10(10), 6063–6081 (2020) https://doi.org/10.1039/C9RA07755C

- [34] Kato, A., Yamamoto, M., Utsuno, F., Higuchi, H., Takahashi, M.: Lithium-ion-conductive sulfide polymer electrolyte with disulfide bond-linked PS4 tetrahedra for all-solid-state batteries. Communications Materials **2**(1), 112 (2021) https://doi.org/10.1038/s43246-021-00216-0
- [35] Mercier, R., Malugani, J.-P., Fahys, B., Robert, G., Douglade, J.: Structure du tetrathiophosphate de lithium. Acta Crystallographica Section B: Structural Crystallography and Crystal Chemistry 38(7), 1887–1890 (1982) https://doi.org/10.1107/S0567740882007535
- [36] Homma, K., Yonemura, M., Kobayashi, T., Nagao, M., Hirayama, M., Kanno, R.: Crystal structure and phase transitions of the lithium ionic conductor Li3PS4. Solid State Ionics 182(1), 53–58 (2011) https://doi.org/10.1016/j.ssi.2010.10.001
- [37] Toffoli, P., Khodadad, P., Rodier, N.: Structure cristalline de l'hexathiodimétaphosphate d'argent, Ag2P2S6. Acta Crystallographica Section B **34**(12), 3561–3564 (1978) https://doi.org/10.1107/S0567740878011590
- [38] Brockner, W., Becker, R., Eisenmann, B., Schaefer, H.: ChemInform Abstract: CRYSTAL STRUCTURE AND VIBRATIONAL SPECTRA OF CESIUM AND POTASSIUM HEXATHIOMETADIPHOSPHATES CS2P2S6 AND K2P2S6. Chemischer Informationsdienst 16(25) (1985) https://doi.org/10.1002/chin. 198525005
- [39] Hanko, J.A., Sayettat, J., Jobic, S., Brec, R., Kanatzidis, M.G.: A<sub>2</sub> CuP<sub>3</sub> S<sub>9</sub> (A = K, Rb), Cs<sub>2</sub> Cu<sub>2</sub> P<sub>2</sub> S<sub>6</sub>, and K<sub>3</sub> CuP<sub>2</sub> S<sub>7</sub>: New Phases from the Dissolution of Copper in Molten Polythiophosphate Fluxes. Chemistry of Materials 10(10), 3040–3049 (1998) https://doi.org/10.1021/cm980175w
- [40] Dietrich, C., Weber, D.A., Culver, S., Senyshyn, A., Sedlmaier, S.J., Indris, S., Janek, J., Zeier, W.G.: Synthesis, Structural Characterization, and Lithium Ion Conductivity of the Lithium Thiophosphate Li<sub>2</sub> P<sub>2</sub> S<sub>6</sub>. Inorganic Chemistry 56(11), 6681–6687 (2017) https://doi.org/10.1021/acs.inorgchem.7b00751
- [41] Maier, Ludwig., Van Wazer, J.R.: Principles of phosphorus chemistry. xiii. thiophosphate salts and esters. Journal of the American Chemical Society 84(16), 3054–3058 (1962) https://doi.org/10.1021/ja00875a004
- [42] Yamane, H., Shibata, M., Shimane, Y., Junke, T., Seino, Y., Adams, S., Minami, K., Hayashi, A., Tatsumisago, M.: Crystal structure of a superionic conductor, Li7P3S11. Solid State Ionics 178(15-18), 1163–1167 (2007) https://doi.org/10.1016/j.ssi.2007.05.020
- [43] Wolf, G.-U., Meisel, M.: ChemInform Abstract: CHEMISTRY OF PHOS-PHORUS COMPOUNDS WITH ADAMANTANE-LIKE STRUCTURE. VII. PREPARATION AND PROPERTIES OF NONATHIOCYCLOTRIPHOS-PHATE. Chemischer Informationsdienst 14(13) (1983) https://doi.org/10.1002/

#### chin.198313031

- [44] Falius, H., Schliephake, A., Schomburg, D.: Cyclische Thiophosphate, Produkte der Umsetzung von elementarem Phosphor mit Alkylammoniumpolysulfiden. Zeitschrift für anorganische und allgemeine Chemie 611(5), 141–148 (1992) https://doi.org/10.1002/zaac.19926110524
- [45] Eckert, H., Zhang, Z., Kennedy, J.H.: Structural transformation of non-oxide chalcogenide glasses. The short-range order of lithium sulfide (Li2S)-phosphorus pentasulfide (P2S5) glasses studied by quantitative phosphorus-31, lithium-6, and lithium-7 high-resolution solid-state NMR. Chemistry of Materials 2(3), 273–279 (1990) https://doi.org/10.1021/cm00009a017
- [46] Dietrich, C., Koerver, R., Gaultois, M.W., Kieslich, G., Cibin, G., Janek, J., Zeier, W.G.: Spectroscopic characterization of lithium thiophosphates by XPS and XAS a model to help monitor interfacial reactions in all-solid-state batteries. Physical Chemistry Chemical Physics 20(30), 20088–20095 (2018) https://doi.org/10.1039/C8CP01968A
- [47] Minshall, P.C., Sheldrick, G.M.: Pyridinium 2,2,5,5-tetrathio- cyclo di(phosphadithianate), [(pyridine)<sub>2</sub> H]<sub>2</sub><sup>2+</sup> [P<sub>2</sub> S<sub>8</sub> ]<sup>2-</sup>. Acta Crystallographica Section B Structural Crystallography and Crystal Chemistry  $\bf 34$ (4), 1378–1380 (1978) https://doi.org/10.1107/S056774087800566X
- [48] Jones, P.G., Weinkauf, A.: Triethylammonium 3,3,6,6-tetrathioxocyclodi(phosphadithianate) at 178 K. Acta Crystallographica Section C Crystal Structure Communications 47(3), 686–687 (1991) https://doi.org/10.1107/S0108270190009416
- [49] Gruber, H., Müller, U.: Zwei neue cyclische Thioanionen: (PPh<sub>4</sub>)<sub>2</sub> [1,3-P<sub>2</sub> S<sub>8</sub>] und (PPh<sub>4</sub>)<sub>2</sub> [Si<sub>2</sub> S<sub>6</sub> Cl<sub>2</sub>]. Neue Synthesewege zu PPh<sub>4</sub> [PS<sub>2</sub> Cl<sub>2</sub>] und PPh<sub>4</sub> [PS<sub>2</sub> Br<sub>2</sub>]. Zeitschrift für anorganische und allgemeine Chemie  $\bf 623(1-6)$ , 957–961 (1997) https://doi.org/10.1002/zaac.199762301149
- [50] Jandali, M.Z., Eulenberger, G., Hahn, H.: Darstellung und Kristallstruktur des Titan(IV)-thiophosphats(V) Ti $_4$  P $_8$  S $_{29}$ . Zeitschrift für anorganische und allgemeine Chemie  ${\bf 530}(11),\ 144–154\ (1985)\ https://doi.org/10.1002/zaac. 19855301117$
- [51] Togo, A., Tanaka, I.: First principles phonon calculations in materials science. Scripta Materialia 108, 1–5 (2015) https://doi.org/10.1016/j.scriptamat.2015.07.021
- [52] Jun, K., Chen, Y., Wei, G., Yang, X., Ceder, G.: Diffusion mechanisms of fast lithium-ion conductors. Nature Reviews Materials 9(12), 887-905 (2024) https://doi.org/10.1038/s41578-024-00715-9

- [53] Tachez, M., Malugani, J., Mercier, R., Robert, G.: Ionic conductivity of and phase transition in lithium thiophosphate Li3PS4. Solid State Ionics **14**(3), 181–185 (1984) https://doi.org/10.1016/0167-2738(84)90097-3
- [54] Kimura, T., Inaoka, T., Izawa, R., Nakano, T., Hotehama, C., Sakuda, A., Tatsumisago, M., Hayashi, A.: Stabilizing High-Temperature α-Li<sub>3</sub> PS<sub>4</sub> by Rapidly Heating the Glass. Journal of the American Chemical Society 145(26), 14466–14474 (2023) https://doi.org/10.1021/jacs.3c03827
- [55] Liu, Z., Fu, W., Payzant, E.A., Yu, X., Wu, Z., Dudney, N.J., Kiggans, J., Hong, K., Rondinone, A.J., Liang, C.: Anomalous High Ionic Conductivity of Nanoporous  $\beta$ -Li<sub>3</sub> PS<sub>4</sub>. Journal of the American Chemical Society **135**(3), 975–978 (2013) https://doi.org/10.1021/ja3110895
- [56] Xuejian, Q., Taoyuze, L., Zhicheng, Z.: EAC-Net: Real-space Charge Density via Equivariant Atomic Contributions. arXiv (2025). https://doi.org/10.48550/ arXiv.2508.04052
- [57] Ye, C.-Y., Weng, H.-M., Wu, Q.-S.: Con-CDVAE: A method for the conditional generation of crystal structures. Computational Materials Today 1, 100003 (2024) https://doi.org/10.1016/j.commt.2024.100003 arXiv:2403.12478 [cond-mat]
- [58] Mattergen/Checkpoints/Chemical\_system\_energy\_above\_hull at Main · Microsoft-/Mattergen. https://github.com/microsoft/mattergen/tree/main/checkpoints/
- [59] Ong, S.P., Richards, W.D., Jain, A., Hautier, G., Kocher, M., Cholia, S., Gunter, D., Chevrier, V.L., Persson, K.A., Ceder, G.: Python Materials Genomics (pymatgen): A robust, open-source python library for materials analysis. Computational Materials Science 68, 314–319 (2013) https://doi.org/10.1016/j.commatsci.2012. 10.028
- [60] Kresse, G., Furthmüller, J.: Efficiency of ab-initio total energy calculations for metals and semiconductors using a plane-wave basis set. Computational Materials Science 6(1), 15–50 (1996) https://doi.org/10.1016/0927-0256(96)00008-0
- [61] Kresse, G., Furthmüller, J.: Efficient iterative schemes for ab initio total-energy calculations using a plane-wave basis set. Physical Review B 54(16), 11169–11186 (1996) https://doi.org/10.1103/PhysRevB.54.11169
- [62] Kresse, G., Joubert, D.: From ultrasoft pseudopotentials to the projector augmented-wave method. Physical Review B **59**(3), 1758–1775 (1999) https://doi.org/10.1103/PhysRevB.59.1758
- [63] Perdew, J.P., Burke, K., Ernzerhof, M.: Generalized Gradient Approximation Made Simple. Physical Review Letters 77(18), 3865–3868 (1996) https://doi.org/ 10.1103/PhysRevLett.77.3865

- [64] Perdew, J.P., Burke, K., Ernzerhof, M.: Generalized Gradient Approximation Made Simple [Phys. Rev. Lett. 77, 3865 (1996)]. Physical Review Letters **78**(7), 1396–1396 (1997) https://doi.org/10.1103/PhysRevLett.78.1396
- [65] Models/343/DPA-3.1-3M. https://www.aissquare.com/models/
- [66] ACEsuit/Mace. https://github.com/ACEsuit/mace (2025)
- $[67] \begin{tabular}{ll} Mattersim/Pretrained\_models & at & Main & Microsoft/Mattersim. \\ https://github.com/microsoft/mattersim/tree/main/pretrained\_models \\ \end{tabular}$

# Supplementary information for "Chemical-space completeness: a new strategy for crystalline materials exploration"

Fengyu Xie<sup>1†</sup>, Ruoyu Wang<sup>1†</sup>, Taoyuze Lv<sup>1</sup>, Yuxiang Gao<sup>1</sup>, Hongyu Wu<sup>2</sup>, Zhicheng Zhong<sup>1, 2\*</sup>

<sup>1\*</sup>College of Artificial Intelligence and Data Science, Suzhou Institute of Advanced Research, University of Science and Technology of China, 188 Ren'ai Road, Suzhou, 215123, Jiangsu, China.
<sup>2</sup>Suzhou Laboratory, 388 Rueshui Road, Suzhou, 215123, Jiangsu

<sup>2</sup>Suzhou Laboratory, 388 Ruoshui Road, Suzhou, 215123, Jiangsu, China.

\*Corresponding author(s). E-mail(s): zczhong@ustc.edu.cn;
Contributing authors: fengyu\_xie@ustc.edu.cn; ruoyuwang@ustc.edu.cn;
taoyuze.lv@ustc.edu.cn; yuxgao@ustc.edu.cn; wuhy@szlab.ac.cn;
†These authors contributed equally to this work.

#### 1 Supplementary methods

#### 1.1 Structural fingerprint

Local structural fingerprints were computed following the same procedure as in CDVAE[1]. Each atomic site was featurized using the CrystalNNFeaturizer ("ops" preset) implemented in matminer[2], with oxidation states assigned via pymatgen's built-in valence-guessing method[3]. A structure-level fingerprint was then obtained by averaging all site vectors over each dimension. These fingerprints were used to produce the distributions and t-SNE visualizations shown in Supplementary Figure 2.

For analyses focusing on the anionic framework, all Li atoms were removed from the structures before recomputing fingerprints, yielding the t-SNE projection presented in Figure 4a of the main text.

#### 1.2 Anion motif extraction and classification

To identify and categorize distinct thiophosphate anionic motifs within generated Li–P–S structures, we developed a graph-based motif extraction pipeline implemented with pymatgen[3], ASE[4], and NetworkX[5].

Each structure was first converted into a connectivity graph where nodes represent atomic sites and edges represent chemical bonds between P and S atoms (Li atoms were excluded). Interatomic distances were compared against empirical cutoffs of 2.35 Å (P–S), 2.20 Å (S–S), and 2.50 Å (P–P). An undirected graph was constructed using these criteria, yielding a P–S bonding network for each structure. The bond graph was then decomposed into connected components using the NetworkX connected-component algorithm, where each subgraph corresponds to a unique anionic cluster such as  $PS_4^{3-}$  or  $P_2S_6^{4-}$ .

To distinguish topologically distinct motifs, each subgraph was encoded using the Weisfeiler–Lehman (WL) graph hash[6] method, with atomic species as node attributes and bond type (P–S, S–S, P–P) as edge attributes. This ensured an isomorphism-invariant representation, allowing unique identification of anion topologies. Each isolated unique cluster was then re-centered in a cubic box (20 Å) and exported as an ASE Atoms object. All skeletal formulae appearing in Figure 4 of the main text were visualized using a demo version of the Marvin chemical drawing tool[7].

#### 1.3 P-T phase diagram computation details

Finite-pressure and finite-temperature phase diagrams were computed using the finetuned DPA-3 MLFF at  $N_{\rm train}=4050$  as the energy and force evaluator. Structural perturbations and force constants were generated with phonopy[8, 9]. To prevent spurious interactions between periodic images, all structures were scaled to ensure lattice parameters of at least 12Å and approximately equal lengths in each direction.

Within the quasi-harmonic approximation (QHA)[10], phonon frequencies were obtained by scaling lattice parameters from  $0.85 \times a_0$  to  $1.15 \times a_0$  in increments of 0.05. The phonon density of states and mode frequencies were then integrated to compute the Helmholtz free energy F(T,V). Finally, the Gibbs free energy G(T,p) was derived through Legendre transformation in the temperature range 0–600 K and pressure range 0–2 GPa. Phase diagrams at varied temperatures and pressures were then constructed by evaluating the Gibbs free energy convex hulls.

#### 1.4 Ionic conductivity computation details

As a preliminary demonstration of the ionic-conductivity screening capability, we performed molecular dynamics (MD) simulations to estimate Li-ion diffusivity at elevated temperature (700 K) over a short simulation time of 60 ps. The resulting conductivities therefore serve as qualitative indicators rather than quantitative room-temperature values.

MD simulations were carried out in ASE using the non-fine-tuned Mattersim-5M[11] model, which was pretrained on high-temperature and high-pressure datasets and exhibits better numerical stability under such conditions. All simulation cells were scaled to ensure lattice parameters of at least 10  $\hbox{Å}$  and approximately isotropic dimensions.

Each system was equilibrated in the NPT ensemble at 1 bar for 10 ps using a Nosé–Hoover thermostat and a 2 fs timestep, followed by 60 ps of production simulation in the NVT ensemble for diffusivity analysis. Elemental diffusivities were obtained by fitting the mean-squared displacement (MSD) in the final 50 ps of the NVT trajectory according to

$$D_{\text{element}} = \frac{\left\langle ||r_i(t_1) - r_i(t_0)||^2 \right\rangle_{i \in \text{element}}}{6(t_1 - t_0)}.$$
 (1)

The Li-ion conductivity was then calculated from the Einstein relation

$$\sigma_{\rm Li} = \frac{n_{\rm Li} z_{\rm Li}^2 e^2 D_{\rm Li}}{k_{\rm B} T},\tag{2}$$

where  $n_{\text{Li}}$  is the Li atomic number density and  $z_{\text{Li}} = 1$ .

#### 1.5 Electronic structure prediction details

The Equivariant Atomic Contribution Network (EAC-Net) was employed to predict electronic charge densities. Specifically, we adopted the pretrained EAC-mp model developed in previous work[12], which was trained on 48,183 CHGCAR files randomly sampled from the Materials Project (MP) database[13]. The model utilized an angular momentum cutoff of  $l_{\rm max}=5$  and a feature dimension of 36. The cutoff radii for atomic and grid representations were set to 4.0 Å and 6.0 Å, respectively, yielding a total of approximately 3.08 million trainable parameters. Comprehensive details on dataset composition, model architecture, training procedures and error quantification can be found in the original EAC-Net publication.

For fine-tuning, we selected 5, 10, 15, 19, and 34 LPS frames from iterations 1 and 2 to evaluate convergence of the model loss with respect to the number of fine-tuning configurations. Each model was trained for 2000 steps with a batch size of 50, using a learning rate decaying monotonically from  $1 \times 10^{-4}$  to  $8 \times 10^{-6}$ . Ten test configurations were selected from iteration 6 for validation.

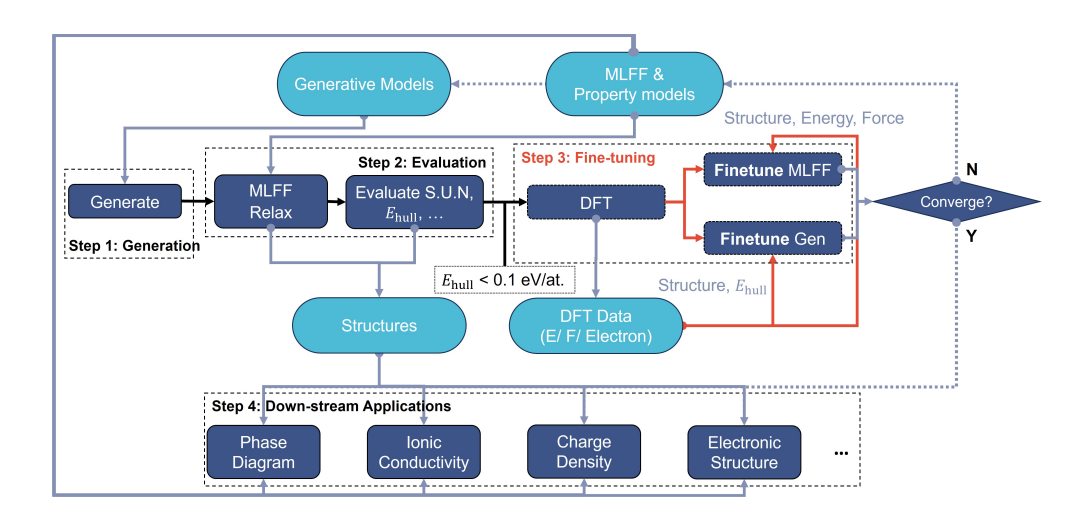
Self-consistent-field (SCF) and non-self-consistent-field (NSCF) DFT calculations were performed using the same computational parameters as those employed for MLFF dataset generation, except that the electronic convergence threshold was tightened to  $10^{-5}$  eV, and the k-point linear density (KSPACING) was increased to 0.2 to ensure the accuracy of the charge-density results.

## 2 Supplementary tables

Table 1 Summary of Li-ion conductor candidates discovered by conductivity screening.  $v_{\rm atom}$  represents specific volume per atom,  $\sigma_{\rm Li,700~K}$  represents Li-ion conductivity at 700 K, and  $E_{\rm hull}$  represents the energy above hull evaluated using the fine-tuned DPA-3. (\*) Same anion arrangement as the α-phase[14]. (#) β-structure, entry from MP database. (!) Li<sub>7</sub>P<sub>3</sub>S<sub>11</sub>, entry from MP database.

Iteration	Name	Formula	$v_{\rm atom}~({\rm \AA}^3/{\rm atom})$	$\sigma_{\mathrm{Li,700~K}}~(\mathrm{mS/cm})$	$E_{\rm hull}~({\rm meV/atom})$
3	ea_0.00_gen_2866(*)	$Li_3PS_4$	21.8	1872.5	28.8
2	$ea_0.00_gen_1016$	$Li_2PS_3$	21.2	1775.9	17.3
1	$ea_0.03_gen_2999$	$Li_2PS_3$	21.4	1490.2	10.7
0	mp-985583-GGA(#)	$Li_3PS_4$	21.8	1397.6	20.6
1	$ea_0.00_gen_2765(*)$	$Li_3PS_4$	22.1	1282.8	24.3
2	ea_0.00_gen_1404	$Li_3PS_4$	23.1	1198.2	29.6
3	$ea_0.06_gen_823$	$Li_3PS_4$	26.1	1163.1	23.3
2	ea_0.00_gen_1607(*)	$Li_3PS_4$	21.9	1142.8	20.0
0	mp-641703-GGA(!)	$\mathrm{Li}_{7}\mathrm{P}_{3}\mathrm{S}_{11}$	22.4	1059.9	28.9
5	$ea_0.03_gen_2294$	$LiPS_4$	32.1	1025.6	27.5
1	$ea_0.00_gen_1603$	$\text{Li}_2\text{P}_2\text{S}_7$	31.5	952.1	24.7
3	$ea_0.03_gen_1068$	$LiPS_3$	28.0	951.2	29.0
1	$ea_0.06_gen_410$	$Li_2PS_3$	20.8	921.1	19.9
1	$ea_0.03_gen_3012$	$Li_2PS_3$	24.1	826.6	21.4
1	$ea_0.03_gen_1288$	$\mathrm{Li}_{7}\mathrm{P}_{3}\mathrm{S}_{10}$	22.1	825.6	25.3
2	$ea_0.00_gen_468$	$LiPS_3$	27.7	819.6	22.6
3	$ea_0.00_gen_371$	$LiPS_3$	30.5	758.5	24.2
1	$ea_0.00_gen_270$	$LiPS_3$	26.7	745.9	24.0
1	$ea_0.03_gen_701$	$Li_2PS_3$	20.7	682.2	19.6
3	$ea_0.06_gen_2550$	$LiPS_4$	30.7	671.6	23.2
1	$ea_0.00_gen_1470$	$Li_2PS_3$	20.9	625.7	9.6
5	$ea_0.06_gen_1312$	$LiPS_4$	40.0	575.1	28.1
1	$ea_0.06_gen_1779$	$Li_2PS_3$	20.6	498.7	23.3
3	$ea_0.03_gen_1953$	$\text{Li}_2\text{P}_2\text{S}_7$	37.5	471.2	28.2
4	$ea_0.06_gen_1317$	$LiPS_4$	34.0	462.2	21.4
2	$ea_0.00_{gen_538}$	$\text{Li}_2\text{P}_2\text{S}_7$	34.2	444.7	25.0
1	$ea_0.00_gen_2221$	$LiPS_4$	31.2	443.0	29.9
1	$ea_0.03_gen_420$	$LiPS_3$	26.9	436.1	17.4
7	$ea_0.00_gen_493$	$LiPS_4$	34.5	435.4	15.2
7	$ea_0.03_gen_3148$	$LiPS_3$	31.7	428.8	18.7
6	$ea_0.00_{gen_1281}$	$LiPS_4$	36.5	406.4	21.3

## 3 Supplementary figures



 ${\bf Fig.~1}~{\bf Schematic~illustration~of~the~iterative~generation-evaluation~workflow~for~crystal~structure~exploration~within~a~defined~chemical~space.$ 

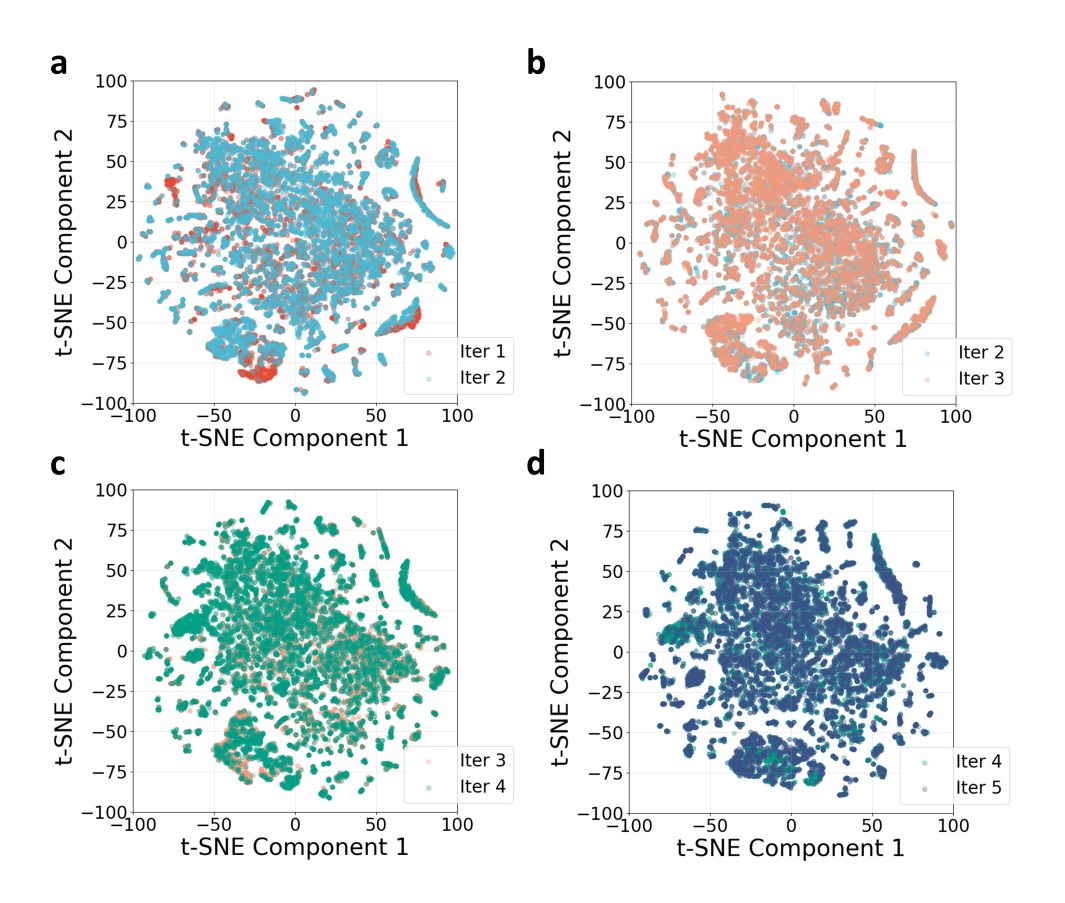


Fig. 2 Comparison of the first two t-SNE components of structural fingerprints between (a) iterations 1 and 2, (b) iterations 2 and 3, (c) iterations 3 and 4, and (d) iterations 4 and 5. The t-SNE features were computed by jointly embedding all generated structures across iterations to ensure alignment, and then plotted every two iterations for comparison.

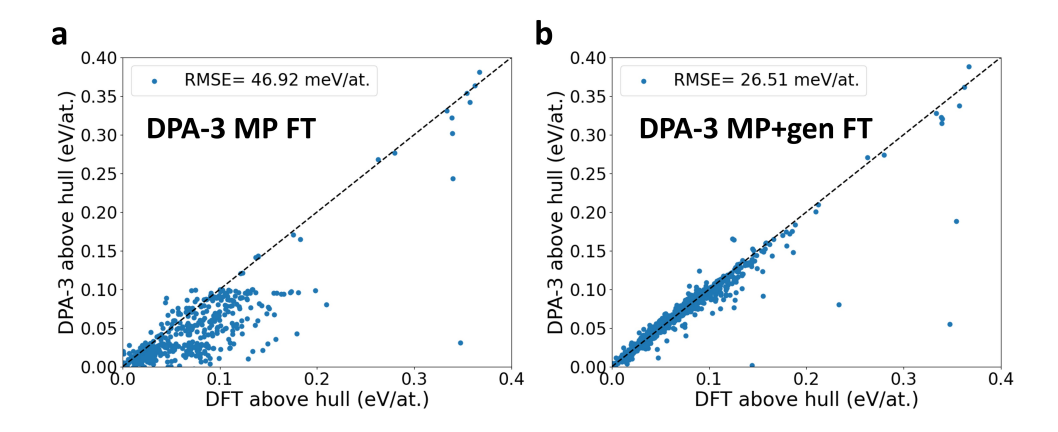


Fig. 3 Parity plots comparing DPA-3 predicted energies above hull with DFT-computed values: (a) fine-tuned using only Li–P–S structures from the MP dataset, and (b) fine-tuned using combined MP and generated data at  $N_{\rm train}=4050$ .

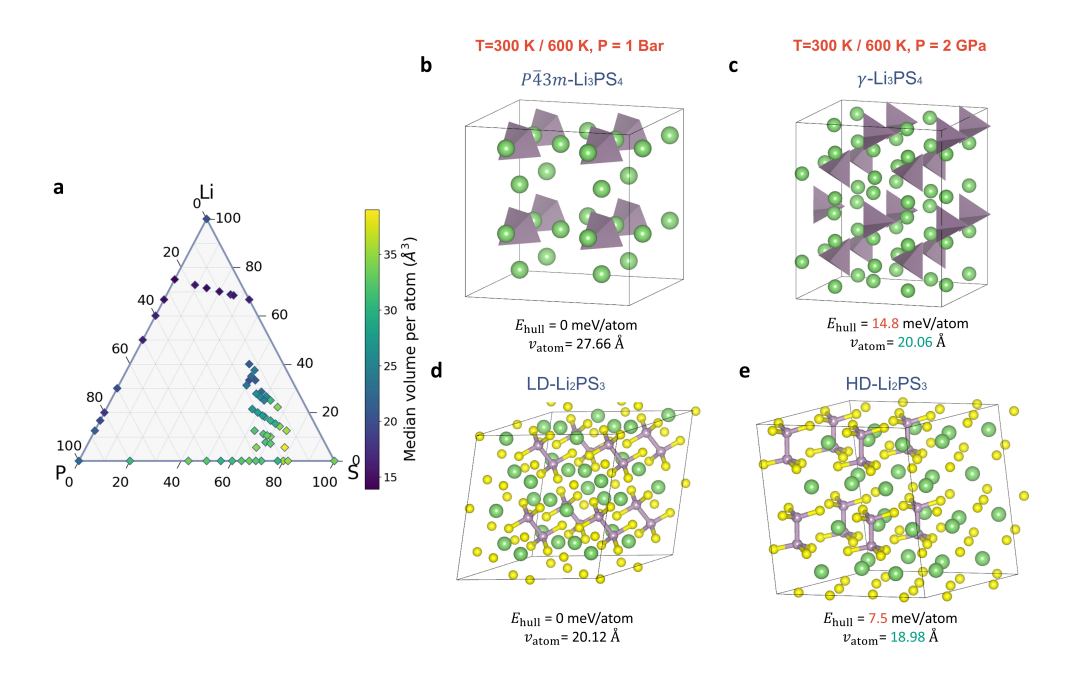
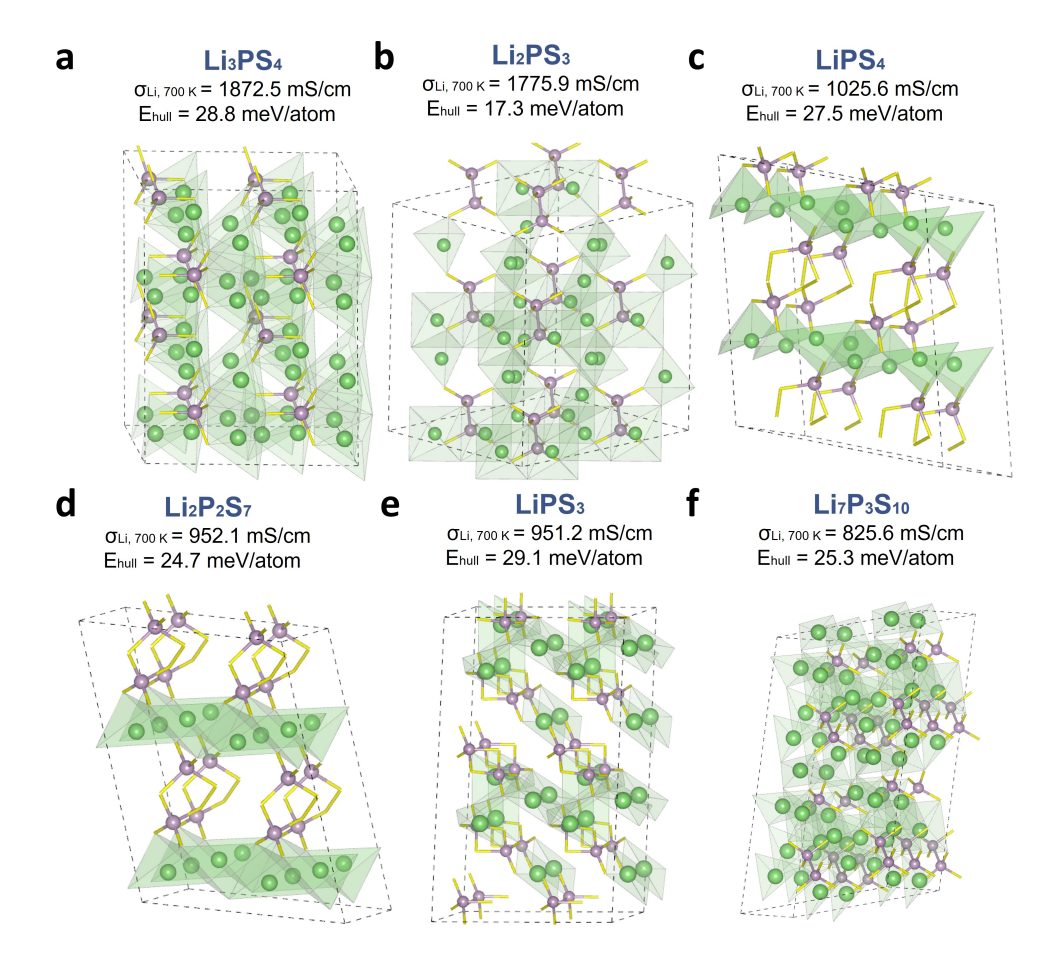
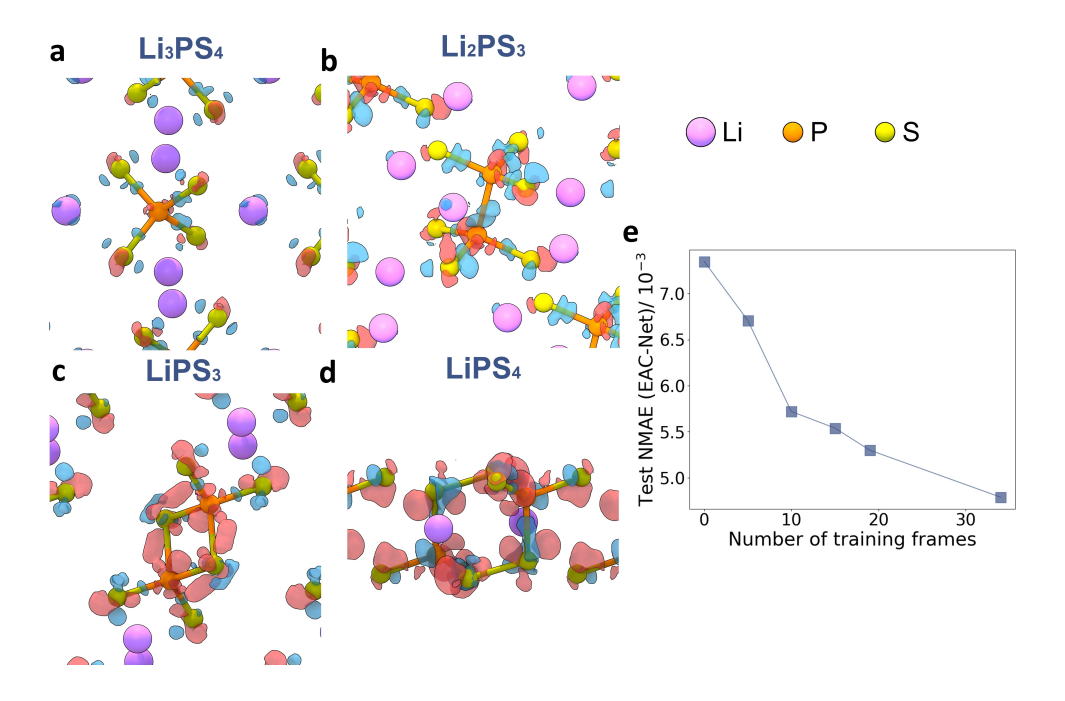


Fig. 4 (a) Median specific volume per atom as a function of composition in the Li–P–S ternary system. Darker blue dots indicate denser atomic packing. (b–c) Lowest Gibbs free-energy structures of Li<sub>3</sub>PS<sub>4</sub> at T=300–600 K under (b) 1 bar (high-symmetry P̄43m phase) and (c) 2 GPa (the  $\gamma$  phase[14]). (d–e) Lowest Gibbs free-energy structures of Li<sub>2</sub>PS<sub>3</sub> at T=300–600 K under (d) 1 bar (low-density, LD phase) and (e) 2 GPa (high-density, HD phase).



**Fig. 5** Crystal structures of representative Li-ion conductors listed in Table 1. Green spheres and transparent polyhedra denote Li ions and their coordination environments, respectively, purple spheres represent P atoms, and purple—yellow sticks indicate P–S bonds. S atoms are omitted for clarity.



**Fig. 6** (a–d) Differences between charge densities predicted by EAC-Net and those computed by DFT for (a)  $\text{Li}_3\text{PS}_4$ , (b)  $\text{Li}_2\text{PS}_3$ , (c)  $\text{Li}_2\text{PS}_3$ , and (d)  $\text{Li}_2\text{PS}_4$ , corresponding to the order in Figure 7 of the main text. (e) Normalized mean absolute error (NMAE) of the predicted charge density as a function of the number of fine-tuning frames.

#### References

- [1] Xie, T., Fu, X., Ganea, O.-E., Barzilay, R., Jaakkola, T.S.: Crystal Diffusion Variational Autoencoder for Periodic Material Generation. In: International Conference on Learning Representations (2021)
- [2] Ward, L., Dunn, A., Faghaninia, A., Zimmermann, N.E.R., Bajaj, S., Wang, Q., Montoya, J., Chen, J., Bystrom, K., Dylla, M., Chard, K., Asta, M., Persson, K.A., Snyder, G.J., Foster, I., Jain, A.: Matminer: An open source toolkit for materials data mining. Computational Materials Science 152, 60–69 (2018) https://doi.org/10.1016/j.commatsci.2018.05.018
- [3] Ong, S.P., Richards, W.D., Jain, A., Hautier, G., Kocher, M., Cholia, S., Gunter, D., Chevrier, V.L., Persson, K.A., Ceder, G.: Python Materials Genomics (pymatgen): A robust, open-source python library for materials analysis. Computational Materials Science 68, 314–319 (2013) https://doi.org/10.1016/j.commatsci.2012. 10.028
- [4] Larsen, A.H., Mortensen, J.J., Blomqvist, J., Castelli, I.E., Christensen, R., Dułak, M., Friis, J., Groves, M.N., Hammer, B., Hargus, C., Hermes, E.D., Jennings, P.C., Jensen, P.B., Kermode, J., Kitchin, J.R., Kolsbjerg, E.L., Kubal, J., Kaasbjerg, K., Lysgaard, S., Maronsson, J.B., Maxson, T., Olsen, T., Pastewka, L., Peterson, A., Rostgaard, C., Schiøtz, J., Schütt, O., Strange, M., Thygesen, K.S., Vegge, T., Vilhelmsen, L., Walter, M., Zeng, Z., Jacobsen, K.W.: The atomic simulation environment—a Python library for working with atoms. Journal of Physics: Condensed Matter 29(27), 273002 (2017) https://doi.org/10.1088/1361-648X/aa680e
- [5] Hagberg, A.A., Schult, D.A., Swart, P.J.: Exploring Network Structure, Dynamics, and Function using NetworkX. In: Python in Science Conference, Pasadena, California, pp. 11–15 (2008). https://doi.org/10.25080/TCWV9851
- [6] Shervashidze, N., Schweitzer, P., Leeuwen, E.J., Mehlhorn, K., Borgwardt, K.M.: Weisfeiler-Lehman Graph Kernels. Journal of Machine Learning Research 12(77), 2539–2561 (2011)
- [7] Marvin Chemical Drawing Software. https://chemaxon.com/marvin
- [8] Togo, A., Chaput, L., Tadano, T., Tanaka, I.: Implementation strategies in phonopy and phono3py. Journal of Physics: Condensed Matter 35(35), 353001 (2023) https://doi.org/10.1088/1361-648X/acd831
- [9] Togo, A.: First-principles Phonon Calculations with Phonopy and Phono3py.
   Journal of the Physical Society of Japan 92(1), 012001 (2023) https://doi.org/10.7566/JPSJ.92.012001
- [10] Togo, A.: First-principles phonon calculations of thermal expansion in Ti3SiC2,

- Ti3AlC2, and Ti3GeC2. Physical Review B **81**(17) (2010) https://doi.org/10. 1103/PhysRevB.81.174301
- [11] Mattersim/Pretrained\_models at Main · Microsoft/Mattersim. https://github.com/microsoft/mattersim/tree/main/pretrained\_models
- [12] Xuejian, Q., Taoyuze, L., Zhicheng, Z.: EAC-Net: Real-space Charge Density via Equivariant Atomic Contributions. arXiv (2025). https://doi.org/10.48550/arXiv.2508.04052
- [13] Jain, A., Ong, S.P., Hautier, G., Chen, W., Richards, W.D., Dacek, S., Cholia, S., Gunter, D., Skinner, D., Ceder, G., Persson, K.A.: Commentary: The Materials Project: A materials genome approach to accelerating materials innovation. APL Materials 1(1), 011002 (2013) https://doi.org/10.1063/1.4812323
- [14] Homma, K., Yonemura, M., Kobayashi, T., Nagao, M., Hirayama, M., Kanno, R.: Crystal structure and phase transitions of the lithium ionic conductor Li3PS4. Solid State Ionics 182(1), 53–58 (2011) https://doi.org/10.1016/j.ssi.2010.10.001